
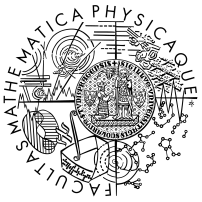

CHARLES UNIVERSITY
Faculty of mathematics
and physics

# Gravitational Lensing:

# From Planets to Galaxy Clusters

Habilitation thesis

**David Heyrovský**

Institute of Theoretical Physics

Prague 2021

## Acknowledgments

The original research papers included in the presented thesis are the outcome of collaboration with my former and current students, Kamil Daněk, Lukáš Ledvina, Lukáš Timko, and Michal Karamazov. Without their skill, invention, and hard work much of the results would never have been achieved. I appreciate not only their contributions to the work, but also their companionship on the twisting and winding scientific journey. I am equally grateful to all my other students who have collaborated on topics not included here. I thank my colleagues at the Institute of Theoretical Physics for cultivating the friendly, open, and intellectually inspiring atmosphere that has been a hallmark of the institute. I am grateful to all my family for being a constant source of support. Most of all, I thank Šárka, Jasmína, and Evelína, for always keeping my spirits up and my feet on the ground.

# Contents


**1 Introduction** . . . . . **1**

**2 Gravitational Lensing Concepts** . . . . . **5**

2.1 Setting the Scene . . . . . 5

2.2 Lens Equation and Lens Characteristics . . . . . 7

2.3 Lens Potential Derivatives and Image Geometry . . . . . 11

**3 Lensing By a Point Mass** . . . . . **13**

3.1 Lens Equation and the Einstein Radius . . . . . 13

3.2 Point-source Images and Their Properties . . . . . 15

3.3 Images of an Extended Source . . . . . 17

3.4 Point-mass-lens Convergence, Shear, and Phase . . . . . 19

**4 Microlensing By Stars and Planets in Our Galaxy** . . . . . **21**

4.1 Microlensing by Single Stars . . . . . 21

4.2 Microlensing by Binary Stars and by Stars with a Planet . . . . . 26

4.3 Microlensing by Three-body Lenses . . . . . 34

4.4 Included Papers on Triple Lenses . . . . . 36

**5 Lensing By Galaxies** . . . . . **39**

5.1 Galaxies as Gravitational Lenses . . . . . 39

5.2 Strong Lensing . . . . . 40

5.3 Quasar Microlensing . . . . . 43

5.4 Included Paper on Quasar Microlensing . . . . . 46

**6 Lensing By Clusters of Galaxies** . . . . . **47**

6.1 Galaxy Clusters as Gravitational Lenses . . . . . 47

6.2 Weak Lensing and Cluster Mass Reconstruction . . . . . 49

6.3 Included Papers on Cluster Lensing . . . . . 51

**7 Conclusions** . . . . . **53**

**References** . . . . . **55**

**A Image-plane Analysis of $n$-Point-mass Lens Critical Curves and Caustics** **63**

**B Critical Curves and Caustics of Triple-lens Models** . . . . . **65**

**C Triple-lens Gravitational Microlensing: Critical Curves for Arbitrary Spatial Configuration** . . . . . **67**

**D X-Ray Line Profile Variations during Quasar Microlensing** . . . . . **69**

**E Gravitational Lensing By a Massive Object in a Dark Matter Halo. I. Critical Curves and Caustics** . . . . . **71**

**F Gravitational Lensing By a Massive Object in a Dark Matter Halo. II. Shear, Phase, and Image Geometry** . . . . . **73**

# Chapter 1

## Introduction

The effect of gravitational lensing occurs in many different astrophysical settings. All involve light from a background source passing on its way to the observer through the gravitational field of a foreground object. If the foreground object is sufficiently massive, sufficiently compact, and sufficiently aligned with the line of sight to the background source, the observer may detect various lensing phenomena caused by gravitational deflection of light: magnification and distortion of the observed source, amplification of its flux, and possibly even multiple imaging.

Since its theoretical prediction in the 1930s (Einstein 1936; Zwicky 1937), it took gravitational lensing more than four decades to enter the realm of observational astronomy. The announcement of the discovery of a doubly imaged quasar by Walsh et al. (1979) started its progression from being a mere novelty to its current role of a versatile and often unique astrophysical tool. Observations of gravitational lensing effects have been used since then for a wide range of objectives, from the detection of exoplanets around stars nearly as far as the Galactic center to the mapping of the total matter distribution in galaxy clusters.

More recent studies, kicked off by the COSMOS project (Massey et al. 2007), use weak gravitational lensing in combination with source redshifts to measure "three-dimensional" maps of the cosmological large-scale structure. Analyses of the gravitational lensing effect on the small-angular-scale anisotropies of the cosmic microwave background measured by the PLANCK mission yielded low-resolution all-sky maps of the dark matter distribution (Planck Collaboration 2014, 2020). Upcoming weak-lensing surveys will utilize terrestrial and space telescopes including the Vera C. Rubin Observatory, Euclid, and the Nancy Grace Roman Space Telescope

to generate 3D high-resolution maps of the overall cosmological matter distribution out to the faintest detectable galaxies. For an overview of gravitational lensing and its diverse applications we recommend the books by Schneider et al. (1992), Schneider et al. (2006), Dodelson (2017), and Congdon & Keeton (2018). This lineup of also provides an illustration of the evolution of the field over three decades. As a complement, Petters et al. (2001) provide more mathematical background for the theory of gravitational lensing.

The presented thesis compiles our contributions to gravitational lensing research from recent years. The six papers included in the appendices range from 2015 to 2021, with the last two included still in the form of preprints. They cover topics from three distinct areas, each studied with different students: Galactic microlensing by three-body lenses with Kamil Daněk, microlensing of quasar X-ray emission with Lukáš Ledvina, and the lensing impact of small-scale substructure in galaxy-cluster lenses with Michal Karamazov and Lukáš Timko. In the following paragraphs we indicate our motivations to study these topics.

By the time of writing, gravitational microlensing surveys and follow-up collaborations have published the analyses of 11 events with clear detections of lensing by three-body systems, as described further in Section 4.3. Four of them involved stars with two planets, and seven of the lenses were binary stars with a planet. It is very likely that more such events could be found in the data archives of the projects. However, the analysis of their light curves is complicated by the lack of insight into the diversity of their structures, which is driven by the geometry of triple-lens caustics and critical curves. Our work on triple lenses was driven by an effort to identify their different lensing regimes and to give a comprehensive overview of their critical-curve topologies and caustic structures. Three papers describing our results are included in Appendices A, B, and C.

One of the intriguing aspects of quasar microlensing, in which microlensing by stars in a lens galaxy modulates the brightness of a lensed quasar image, is its sensitivity to the surface brightness distribution of the quasar accretion disk. The measured light curve could thus be used to resolve the emitting region of the quasar. Its brightness distribution could be studied in a similar way as in the case of the source stars in Galactic microlensing caustic-crossing events, as shown in our previous work (Heyrovský 2003; Fouqué et al. 2010; Heyrovský &

Sasselov 2000; Heyrovský et al. 2000). In the case of quasar microlensing in the optical regime, the size of the emitting region is often comparable or larger than the local structures of the caustic network. The microlensing light curve is then affected by a degenerate combination of the brightness distribution on the source and the local caustic-network structure of the lens. However, since the size of the emitting region is generally smaller for shorter wavelengths (Alloin et al. 2006), in X-rays microlensing can be described by simple fold-caustic crossings, using local linear approximations of the caustic. Since hard X-ray emission from quasars often features a prominent iron K$\alpha$ line, X-ray spectroscopy could reveal changes in its line profile as observed by Chartas et al. (2012). Our goal was to study microlensing variations in the spectral line profile based on simulations using a relativistic model of emission from the central region of the quasar accretion disk. The results of our study are presented in the paper in Appendix D.

Arguably the most impressive outcome of galaxy-cluster lensing research is the mapping of their total matter distribution. Current cluster mass reconstructions combine weak-lensing mapping with a strong lensing analysis of the inner region of the cluster, individually treating detected strong lensing by cluster-member galaxies. One of the ongoing goals of such reconstructions is to increase the spatial resolution of these maps to detect smaller substructures in the matter distribution. This would provide observational data on their abundance, which could be compared with the results of cosmological structure-formation simulations. Within the galaxy-cluster environment, substructures that could be revealed by their lensing signature include dim cluster galaxies (with low surface brightness or small size), isolated dark-matter subhalos or other concentrations, or possibly even isolated wandering supermassive black holes. The objective of our research was to take a bottom-up approach and first study the lensing influence of a single massive object in the dark-matter halo of the cluster. The low number of parameters of such a simple model permits a detailed systematic study of its properties. Two papers describing our results are included in Appendices E and F.

The introductory Chapters 2–6 are intended neither as a review, nor as a text-book-style exposition. Their purpose is to provide a brief introduction to gravitational lensing and its concepts that are explored in the included papers. Chapter 2 describes the basic setting of gravitational lensing and introduces the "tools of the trade", starting with the lens equation

and ending with lens convergence, shear, and phase. These concepts are illustrated in Chapter 3 for the fundamental gravitational lens model, that of a point-mass lens. The model is not merely an academic exercise; it can be used to describe microlensing by stars in our Galaxy. A combination of two point masses can be used to describe microlensing by binary stars or by stars with a planet. A combination of three point masses can describe microlensing by a star with two planets, or even a star with a planet with a moon. Galactic microlensing by such lenses is discussed in Chapter 4. Larger systems such as galaxies are better described by continuous matter distributions. Strong lensing by galaxies, and the role of their stellar populations in quasar microlensing are the subjects of Chapter 5. Galaxy clusters exhibit a range of lensing phenomena at different scales, as discussed in Chapter 6. In particular, the analysis of their weak lensing provides a means to map their total mass distribution. We conclude in Chapter 7 by commenting on directions of further research on the presented topics.

# Chapter 2

## Gravitational Lensing Concepts

### 2.1 Setting the Scene

The astrophysical setup of gravitational lensing involves an observer, a background source of light or, more generally, electromagnetic radiation (the "source" in lensing terminology), and a massive foreground object closely aligned with the line of sight to the source (the "lens" in lensing terminology). Due to deflection of light in the gravitational field of the lens the observer does not see the source at the same position as in the absence of the lens. Instead, the observer sees one or more images with different brightness and shape in directions displaced from the direction to the source. This simple scenario opens up the broad field of gravitational lensing research, which studies the connection between the properties of the images, of the lens, and of the source. Depending on the specific astrophysical objects involved, observations of image position, shape, and their possibly variable brightness can reveal unique information on the structure of the lens and the source.

A rigorous physical analysis of the described setup would involve studying the propagation of electromagnetic waves in the space-time metric corresponding to the matter distribution of the specific lens in a given cosmological background. In addition, the source, lens, and observer move along their general trajectories, and the source emission and the lens configuration may vary with time. Tackling the initially simple setup in its full generality suddenly looks, and is, daunting. Fortunately, several approximations and assumptions relevant to most scenarios of interest can be made to reduce the analysis to a computationally feasible level. For example,

the assumption of geometric optics replaces the study of wave propagation by the study of photon geodesics, light rays, and light-ray bundles. The justification is non-trivial only in the vicinity of lens caustics, where diffraction patterns arise in wave optics (Herlt & Stephani 1976; Deguchi & Watson 1986; Nye 1999). However, even there, detecting deviations from geometric optics would require (near-)monochromatic observations of extremely compact sources of coherent emission, such as pulsars in distant galaxies (Schneider et al. 1992). Typical gravitational lensing observations involve broad-band observations of lensed quasars, galaxies, or non-degenerate stars in our Galaxy, for all of which the assumption is justified.

In typical gravitational lensing, the lens is associated neither with the source nor with the observer, both of which are asymptotically distant from it. The light ray can then be replaced by its incoming and outgoing asymptotes, i.e., straight lines at local scales or photon geodesics at cosmological scales. The influence of the lens merely causes the (oriented) deflection angle between them. We note that this approximation is not valid for example in the case of "self-lensing" of emission from accretion disks by their central black hole. Neither can it be assumed in cosmic shear studies, which explore the lensing effect of the full cosmological matter distribution between the source and the observer.

These cases also naturally form the main exceptions to the widely used thin-lens approximation, in which the line-of-sight depth of the matter distribution of the lens is negligible in comparison with the distances between the observer, lens, and source. The lens is thus considered to lie at a single distance from the observer, which defines the lens plane (or image plane) perpendicular to the line of sight. The source plane is defined analogously as the plane perpendicular to the line of sight at the distance of the source. In the thin-lens approximation, the three-dimensional density distribution of the lens can be integrated along the line of sight to yield the two-dimensional column density (or surface density) in the lens plane. The amplitude and orientation of the deflection angle is then a function of the position at which the light ray passes through the lens plane.

The lens is generally assumed to be in a quasi-static configuration, meaning that its structure does not change significantly on the light-deflection timescale. For example, for a compound lens with orbiting components this requires non-relativistic orbital velocities. The lensing by

such a lens with internal motions can then be studied as a quasi-static sequence of lensing by lenses with different two-dimensional projected configurations. Finally, the lensing is usually described in the rest frame of the (center of mass) of the lens. For similar reasons as in the case of internal lens motions, the relative velocities of the observer, lens, and source, are usually assumed to be non-relativistic. Nevertheless, constant relativistic velocities are straightforward to account for by Lorentz transformations, which merely introduce a velocity dependence of the lensing parameters (Heyrovský 2005).

## 2.2 Lens Equation and Lens Characteristics

Under the assumptions described in Section 2.1, gravitational lensing can be illustrated by the sketch in Figure 2.1. The observer (O) observes light from the source (S) at a distance $D_\mathrm{s}$. En route to the observer the light is deflected by the lens (L) at a distance $D_\mathrm{l}$ from the observer and $D_\mathrm{ls}$ from the source. Details of specific lensing situations are usually studied in the depicted lens and source planes, which are perpendicular to the line of sight passing from the observer through the lens position toward the source.

Positions in the source and lens planes are customarily divided by their respective distances from the observer, yielding angular positions in radians. In Figure 2.1, a light ray marked by the solid red line originates from point S at position $\boldsymbol{\beta}$, which lies in the source plane at an angular separation $|\boldsymbol{\beta}|$ from the line of sight to the lens. The light ray passes through a point at position $\boldsymbol{\theta}$ in the lens plane, where it is deflected by an angle $\boldsymbol{\alpha}(\boldsymbol{\theta})$ toward the observer. The observer thus sees an image I in the direction $\boldsymbol{\theta}$, displaced from the direction $\boldsymbol{\beta}$ to the source.

At a local, Galactic scale, the line-of-sight distances $D_\mathrm{s}$, $D_\mathrm{l}$, and $D_\mathrm{ls}$ can be approximated by simple coordinate distances. At a cosmological scale, the distances correspond to the respective angular diameter distances. At either scale, the angles $\beta, \theta, \alpha$ in typical gravitational lensing settings are tiny ($\lesssim 10^{-4}$ even for galaxy-cluster lensing), so that we may replace projected perpendicular distances in the source plane by arc lengths. The projected triangle marked in the source plane in Figure 2.1 illustrates the gravitational lens equation,

$$\boldsymbol{\beta} = \boldsymbol{\theta} - \frac{D_\mathrm{ls}}{D_\mathrm{s}}\,\boldsymbol{\alpha}(\boldsymbol{\theta})\,, \tag{2.1}$$

which connects the position of the source $\boldsymbol{\beta}$ with the position of its image $\boldsymbol{\theta}$. Note that if

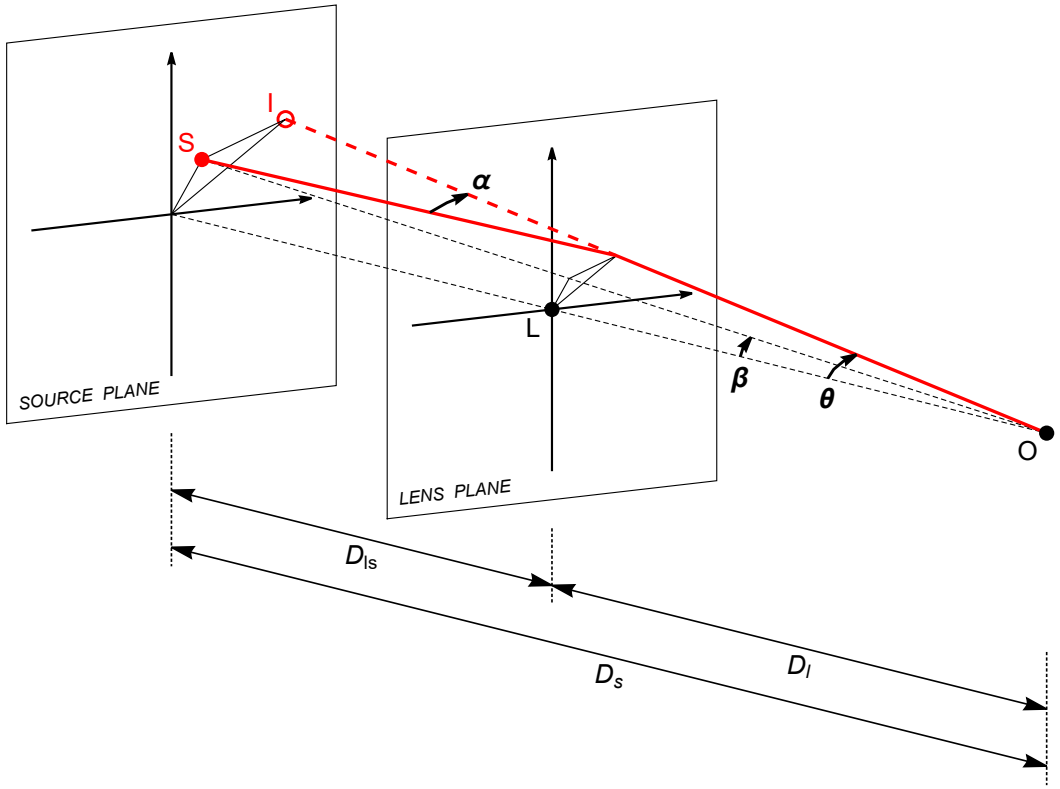


**Figure 2.1:** Gravitational lensing configuration. Bullets: positions of the observer (O), the lens (L), the source (S), and the image (I). Solid red line: light ray from source to observer; dashed red line: direction to image perceived by observer. Denoted angles: angular displacement of the source ($\boldsymbol{\beta}$) and the image ($\boldsymbol{\theta}$) from the line of sight to the lens; gravitational deflection angle $\boldsymbol{\alpha}$. Line-of-sight distances between the observer and the source and lens planes are marked at the bottom of the figure.

we know the deflection angle $\boldsymbol{\alpha}(\boldsymbol{\theta})$, the lens equation yields a unique source position for a given image position. On the other hand, finding an image position for a given source position requires inverting the lens equation. The number of solutions and, thus, the number of images depends on the source position $\boldsymbol{\beta}$ as well as on the functional form of $\boldsymbol{\alpha}(\boldsymbol{\theta})$.

Several important properties of the images can be found by computing the Jacobian, the determinant of the lens-equation Jacobian matrix:

$$\det J(\boldsymbol{\theta}) = \left| \frac{\partial \boldsymbol{\beta}}{\partial \boldsymbol{\theta}} \right| \tag{2.2}$$

For an image located at $\boldsymbol{\theta} = \boldsymbol{\theta}_0$, the sign of $\det J(\boldsymbol{\theta}_0)$ yields the image parity, which is positive

for regular and negative for mirror images of the source. The inverse of its absolute value, $|\det J(\boldsymbol{\theta}_0)|^{-1}$, yields the point-source magnification at $\boldsymbol{\theta}_0$. Since the magnification of a point source is defined as the ratio of infinitesimal solid angles subtended by the image and by the source, it is also equal to the amplification of flux from the source, i.e., the brightening of the image. The terms "point-source amplification" and "point-source magnification" both describe the same quantity; hence, they are interchangeable. If a source at point $\boldsymbol{\beta}$ has $n$ images at positions $\boldsymbol{\theta}_1, \boldsymbol{\theta}_2, \ldots \boldsymbol{\theta}_n$, its total brightening due to the lens is given by the total point-source amplification, defined as

$$A_0(\boldsymbol{\beta}) = \sum_{i=1}^{n} |\det J(\boldsymbol{\theta}_i)|^{-1} . \tag{2.3}$$

The zero-Jacobian contour plays an important role in gravitational lensing. The set of all points $\boldsymbol{\theta}$ in the lens plane of a particular gravitational lens that satisfy the condition

$$\det J(\boldsymbol{\theta}) = 0 \tag{2.4}$$

forms the critical curve of the lens. The critical curve generally sets the boundary in the lens plane between regions with positive and negative image parities (for a rare exception see Appendix B of Karamazov et al. 2021, included here in Appendix E). By its definition, the point-source magnification of any point-like image lying on the critical curve is infinite. Using the lens equation shown in Equation (2.1) to map the critical curve back to the source plane yields the caustic, another characteristic curve of the lens.

From the perspective of the source plane, points along the caustic may have multiple images forming curves in the lens plane. Those images along which the magnification is divergent form the critical curve of the lens. Since at least one of the images of points $\boldsymbol{\beta}$ on the caustic lies on the critical curve, the total point-source amplification $A_0(\boldsymbol{\beta})$ given by Equation (2.3) is divergent along the caustic of the lens. The divergence is accompanied by a change in the number of images across the caustic (e.g., Schneider et al. 1992). A point on its inner side typically has an additional pair of images in comparison with a point on the outer side of the caustic. The additional pair of images appears or disappears at a point along the critical curve, and thus it causes the divergence of the amplification.

While critical curves appear as zero-level contours in lens-plane maps of the Jacobian (e.g., in the left panel of Figure 2 in Appendix E), caustics appear as "infinite-level" contours in

amplification maps, which are source-plane maps of the total point-source amplification $A_0(\boldsymbol{\beta})$ (e.g., in the right panel of Figure 2 in Appendix E). The amplification divergence along the caustic, which is clearly unphysical, arises from one broken and one unphysical assumption. The first is the assumption of geometric optics, as discussed in Section 2.1, and the second is the point-source assumption.

Any astrophysically relevant source is extended rather than point-like, subtending a possibly very small but nevertheless non-zero solid angle. We mark the position of the source center $\boldsymbol{\beta}_\mathrm{c}$ and the position of a source point relative to the source center $\boldsymbol{\beta}'$. The total amplification of such an extended source can be computed by convolution of the point-source amplification $A_0(\boldsymbol{\beta})$ with the surface brightness (or intensity) distribution $I(\boldsymbol{\beta}')$ of the source, normalized by the flux in absence of the lens:

$$A(\boldsymbol{\beta}_\mathrm{c}) = \frac{\int_{\Sigma_\mathrm{S}} A_0(\boldsymbol{\beta}_\mathrm{c}+\boldsymbol{\beta}')\, I(\boldsymbol{\beta}')\, \mathrm{d}^2\boldsymbol{\beta}'}{\int_{\Sigma_\mathrm{S}} I(\boldsymbol{\beta}')\, \mathrm{d}^2\boldsymbol{\beta}'} = \frac{\int_{\Sigma_\mathrm{I}} I(\boldsymbol{\beta}[\boldsymbol{\theta}]-\boldsymbol{\beta}_\mathrm{c})\, \mathrm{d}^2\boldsymbol{\theta}}{\int_{\Sigma_\mathrm{S}} I(\boldsymbol{\beta}')\, \mathrm{d}^2\boldsymbol{\beta}'}\,. \tag{2.5}$$

The integrals in the first expression and in the denominator of the second expression are computed over the full solid angle $\Sigma_\mathrm{S}$ subtended by the source, and the integral in the numerator of the second expression is computed over the full solid angle $\Sigma_\mathrm{I}$ subtended by all images of the source (Pejcha & Heyrovský 2009). The second expression, which is obtained by transforming the integration to the lens plane and utilizing Equation (2.3), shows that the divergence of $A_0(\boldsymbol{\beta})$ is integrable, yielding finite amplification even for sources crossing the caustic. In many cases, numerical evaluation of the integral in the numerator of the first expression is computationally demanding. In such situations, the amplification may be obtained by methods based on the second expression, such as inverse ray shooting (Kayser et al. 1986) or image-plane integration (Bennett & Rhie 1996; Vermaak 2000; Pejcha & Heyrovský 2009).

Equation (2.5) indicates that for an extended source the amplification is generally not equal to the magnification, i.e., the ratio of solid angles subtended by the images and by the source. The two are equal only for uniform sources with a constant surface brightness distribution, or in cases when the point-source amplification varies little across the surface of the source, so that $A(\boldsymbol{\beta}_\mathrm{c}) \approx A_0(\boldsymbol{\beta}_\mathrm{c})$. Equation (2.5) also indicates that even though gravitational light deflection is independent of wavelength, the amplification of an extended source may depend on wavelength through the combination of two factors. First, the surface brightness distribution

$I(\boldsymbol{\beta}')$ of astrophysical sources is typically wavelength dependent. Second, the emitting area of the source $\Sigma_{\rm S}$ may be wavelength dependent.

## 2.3 Lens Potential Derivatives and Image Geometry

For mass distributions relevant to astrophysical lenses the deflection angle can be expressed as

$$\boldsymbol{\alpha}(\boldsymbol{\theta}) = \frac{D_{\rm s}}{D_{\rm ls}} \nabla_{\boldsymbol{\theta}} \psi(\boldsymbol{\theta}) \,, \tag{2.6}$$

where the image-plane scalar function $\psi(\boldsymbol{\theta})$ is the lens potential (also referred to as lensing or deflection potential in the literature). This expression for the deflection angle can be used in Equation (2.1) to yield the following form of the lens equation:

$$\boldsymbol{\beta} = \boldsymbol{\theta} - \nabla_{\boldsymbol{\theta}} \psi(\boldsymbol{\theta}) \,. \tag{2.7}$$

Its Jacobian matrix can be expressed in the form

$$J(\boldsymbol{\theta}) = \frac{\partial \boldsymbol{\beta}}{\partial \boldsymbol{\theta}} = \begin{pmatrix} 1 - \kappa - \gamma \cos 2\varphi & -\gamma \sin 2\varphi \\ -\gamma \sin 2\varphi & 1 - \kappa + \gamma \cos 2\varphi \end{pmatrix} , \tag{2.8}$$

where $\kappa, \gamma, \varphi$ are combinations of the second partial derivatives of the lens potential. Specifically, the convergence $\kappa$ is defined as

$$\kappa(\boldsymbol{\theta}) = \frac{1}{2} \left( \psi_{,11} + \psi_{,22} \right) , \tag{2.9}$$

the shear $\gamma$ is defined as

$$\gamma(\boldsymbol{\theta}) = \sqrt{\frac{1}{4} \left( \psi_{,11} - \psi_{,22} \right)^2 + \left( \psi_{,12} \right)^2} \,, \tag{2.10}$$

and the phase $\varphi$ is defined in terms of its trigonometric functions as

$$\left[ \cos 2\varphi(\boldsymbol{\theta}), \sin 2\varphi(\boldsymbol{\theta}) \right] = \gamma^{-1} \left[ \frac{1}{2} \left( \psi_{,11} - \psi_{,22} \right) , \psi_{,12} \right] . \tag{2.11}$$

In terms of these quantities, the Jacobian introduced in Equation (2.2) has the simple form

$$\det J(\boldsymbol{\theta}) = \left[ 1 - \kappa(\boldsymbol{\theta}) \right]^2 - \gamma^2(\boldsymbol{\theta}) \,. \tag{2.12}$$

Equation (2.4) then yields an implicit expression for the critical curve,

$$\gamma(\boldsymbol{\theta}) = \left| 1 - \kappa(\boldsymbol{\theta}) \right| . \tag{2.13}$$

The convergence–shear formalism is particularly useful for studying the geometry of images of small sources. We denote the source-center position $\boldsymbol{\beta}_\mathrm{c}$ and concentrate on one of its images appearing at $\boldsymbol{\theta}_\mathrm{c}$. In order to explore the imaging properties of the lens equation, we expand it to linear order in the vicinity of $\boldsymbol{\theta}_\mathrm{c}$. For source points $\boldsymbol{\beta}$ near $\boldsymbol{\beta}_\mathrm{c}$ we get

$$\boldsymbol{\beta} - \boldsymbol{\beta}_\mathrm{c} \approx J(\boldsymbol{\theta}_\mathrm{c})\,(\boldsymbol{\theta} - \boldsymbol{\theta}_\mathrm{c}) \tag{2.14}$$

for image points $\boldsymbol{\theta}$ near $\boldsymbol{\theta}_\mathrm{c}$.

Inverting Equation (2.14), we get

$$\boldsymbol{\theta} - \boldsymbol{\theta}_\mathrm{c} \approx \mathbb{A}(\boldsymbol{\theta}_\mathrm{c})\,(\boldsymbol{\beta} - \boldsymbol{\beta}_\mathrm{c})\,, \tag{2.15}$$

where the inverse matrix of $J(\boldsymbol{\theta})$ has the form

$$\mathbb{A}(\boldsymbol{\theta}) = \frac{1}{[\,1-\kappa\,]^2 - \gamma^2} \begin{pmatrix} 1-\kappa+\gamma\cos 2\varphi & \gamma\sin 2\varphi \\ \gamma\sin 2\varphi & 1-\kappa-\gamma\cos 2\varphi \end{pmatrix}. \tag{2.16}$$

When expressed at the position of the source-center image $\boldsymbol{\theta}_\mathrm{c}$ in Equation (2.15), this constant symmetric matrix causes an expansion or contraction in two perpendicular directions. For a small circular source this generates a small elliptic image. However, note that the factor in the denominator of Equation (2.16) indicates that images appearing close to the critical curve may be substantially magnified. Accounting for larger displacements from $\boldsymbol{\theta}_\mathrm{c}$ in the image plane then requires including higher-order corrections to the linear expansion in Equation (2.14), which cause distortions of the elliptic shape.

For a more detailed analysis of the image geometry as a function of convergence, shear, and phase, see Section 2.3 and Appendix A of Karamazov & Heyrovský (2021), included here in Appendix F. Image distortions play a key role in the regime of weak lensing, discussed in Chapter 6.

# Chapter 3

## Lensing By a Point Mass

### 3.1 Lens Equation and the Einstein Radius

In the simplest model of a gravitational lens, the gravitational field of a massive astrophysical object is described by that of a point mass. In terms of general relativity, the metric of the curved space-time of the lensing object is approximated by the Schwarzschild metric and photons propagate along its null geodesics. The angle between the incoming and outgoing asymptotes to the geodesics can be described by the light-deflection formula

$$\boldsymbol{\alpha}(\boldsymbol{\theta}) = \frac{4\,G\,M}{c^2\,D_{\mathrm{l}}}\,\frac{\boldsymbol{\theta}}{|\boldsymbol{\theta}|^2}\,, \tag{3.1}$$

where $M$ is the mass of the lensing object, $G$ is the gravitational constant, and $c$ is the speed of light. The orientation of the angle reflects the circular symmetry of the simple configuration, in which the entire photon geodesic lies in the plane defined by the observer, source, and the point mass. As shown in Figure 3.1, in such a case the source and image positions, $\boldsymbol{\beta}$ and $\boldsymbol{\theta}$, are parallel.

The formula in Equation (3.1) represents the first post-Newtonian approximation of the deflection angle. This approximation fails for photons passing within a few Schwarzschild radii of compact objects such as neutron stars or black holes. Such photons may reach the observer and form higher-order relativistic images of background sources. Nevertheless, in the context of gravitational lensing their contribution to the observed flux is negligible, due to their near-zero magnification (Virbhadra & Ellis 2000). Hence, Equation (3.1) is a good approximation even for the dominant images formed by neutron-star and black-hole gravitational lenses. The

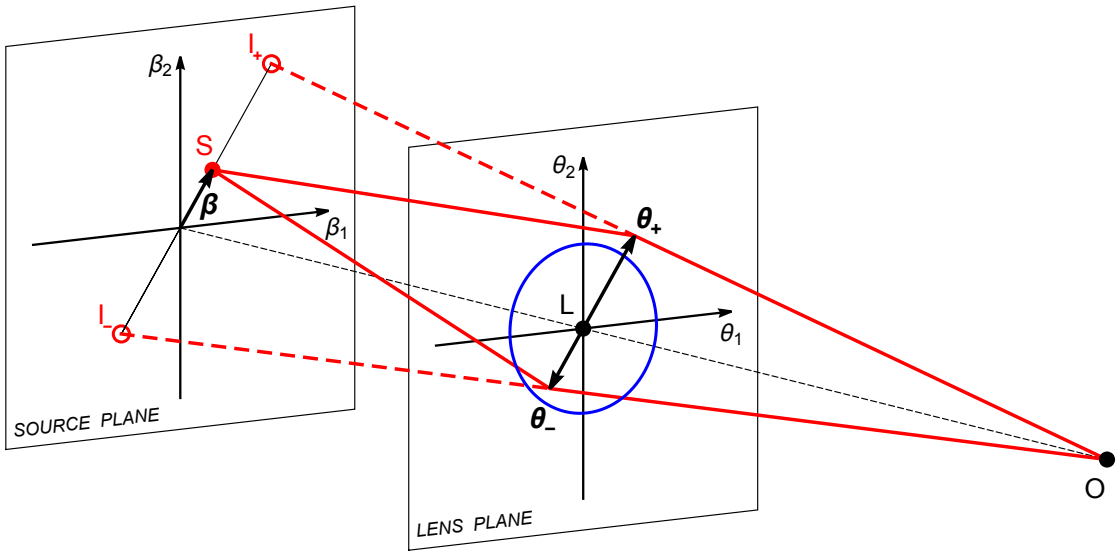


**Figure 3.1:** Gravitational lensing by a point-mass lens. Light from a source at angular position $\boldsymbol{\beta}$ (marked in the source plane) is lensed by a point mass at L, which forms two images perceived by the observer at $I_+$ and $I_-$. Their angular positions are marked in the lens plane: $\boldsymbol{\theta}_+$ lies outside and $\boldsymbol{\theta}_-$ inside the Einstein circle (blue). Remaining notation as in Figure 2.1.

results based on the approximation in this chapter are valid for them as well.

Substituting Equation (3.1) for the deflection angle in Equation (2.1) yields the lens equation for the point-mass lens,

$$\boldsymbol{\beta} = \left(1 - \frac{\theta_\mathrm{E}^2}{\theta^2}\right) \boldsymbol{\theta}\,. \tag{3.2}$$

All the constants and distances appearing in the original equations are combined in a single quantity, the (angular) Einstein radius,

$$\theta_\mathrm{E} = \sqrt{\frac{4\,G\,M}{c^2}\,\frac{D_\mathrm{ls}}{D_\mathrm{s}\,D_\mathrm{l}}}\,. \tag{3.3}$$

The Einstein radius is directly proportional to the square root of the lens mass, inversely proportional to the square root of the lens distance, and directly proportional to the square root of the fractional lens-source distance along the line of sight to the source. Note that for asymptotically distant sources for which $D_\mathrm{s} \gg D_\mathrm{l}$, the Einstein radius is determined purely by the mass of the lens and its distance from the observer, independent of the source.

## 3.2 Point-source Images and Their Properties

Equation (3.2) is simple enough to be inverted analytically, yielding the image position as a function of source position. For a point source at $\beta \neq 0$ the lens forms two images at positions

$$\boldsymbol{\theta}_{\pm} = \left( \frac{1}{2} \pm \sqrt{\frac{1}{4} + \frac{\theta_{\rm E}^2}{\beta^2}} \right) \boldsymbol{\beta} \,, \tag{3.4}$$

both lying in the plane defined by the observer, source, and the point mass (see Figure 3.1). For $\beta = 0$ the source lies directly behind the lens. In this case there is no preferred plane for the light ray and Equation (3.2) shows that the image of the source,

$$\theta^2 = \theta_{\rm E}^2 \,, \tag{3.5}$$

is an Einstein circle around the lens.

Before describing the properties of the two images, we compute the lens-equation Jacobian. We use Equation (3.2) and the definition in Equation (2.2) to obtain

$$\det J(\boldsymbol{\theta}) = 1 - (\theta_{\rm E}/\theta)^4 \,. \tag{3.6}$$

The image at $\boldsymbol{\theta}_+$ lies on the same side of the lens as the source (i.e., $\boldsymbol{\beta} \cdot \boldsymbol{\theta}_+ > 0$); it appears outside the Einstein radius ($\theta_+ > \theta_{\rm E}$) at a larger angular separation from the lens than the source ($\theta_+ > \beta$); it has positive parity ($\det J(\boldsymbol{\theta}_+) > 0$) and it is magnified ($1/|\det J(\boldsymbol{\theta}_+)| > 1$).

The image at $\boldsymbol{\theta}_-$ lies on the opposite side of the lens than the source (i.e., $\boldsymbol{\beta} \cdot \boldsymbol{\theta}_- < 0$); it appears inside the Einstein radius ($\theta_- < \theta_{\rm E}$); it has negative parity ($\det J(\boldsymbol{\theta}_-) < 0$). It is always the less magnified of the two images, $1/|\det J(\boldsymbol{\theta}_-)| < 1/|\det J(\boldsymbol{\theta}_+)|$. Thus, in terms of flux it is always the dimmer of the two. The remaining properties of this image depend on the source position $\beta$. For $\beta > \theta_{\rm E}/\sqrt{2} \approx 0.707\,\theta_{\rm E}$ it lies at a smaller angular separation from the lens than the source ($\theta_- < \beta$), while for $\beta < \theta_{\rm E}/\sqrt{2}$ it lies at a larger angular separation from the lens than the source ($\theta_- > \beta$). For $\beta > \theta_{\rm E}(2^{1/4} - 2^{-1/4}) \approx 0.348\,\theta_{\rm E}$ it is demagnified ($1/|\det J(\boldsymbol{\theta}_-)| < 1$), while for $\beta < \theta_{\rm E}(2^{1/4} - 2^{-1/4})$ it is magnified ($1/|\det J(\boldsymbol{\theta}_-)| > 1$).

The positions of the images for different source positions $\beta$ are also illustrated by the bright yellow dots in the lens-plane plots in Figure 3.2. Here the source (pale yellow dot) is placed for simplicity along the positive sense of the vertical axis, with the $\boldsymbol{\theta}_+$ image lying outside and above the blue Einstein circle, and the $\boldsymbol{\theta}_-$ image lying below the lens inside the Einstein circle.

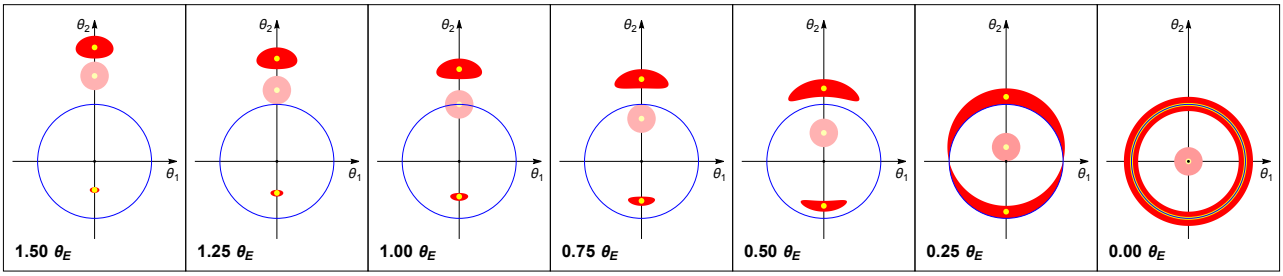


**Figure 3.2:** Extended-source and point-source images formed by a point-mass lens, plotted in the lens plane. The location of the uniformly bright circular source with radius $\beta_\mathrm{r} = 0.25\,\theta_\mathrm{E}$ is indicated by the pale red disk; the point source is illustrated by its center (pale yellow dot). In the presence of the lens (located at the center of the blue Einstein circle), instead of the source one sees its images: bright red for the circular source, bright yellow for its center. Source-center positions $\beta_\mathrm{c}$ are marked at the bottom of the panels. Note the Einstein-ring image at the right, which forms as the two images merge when the lens caustic lies on the source (for $\beta_\mathrm{c} < \beta_\mathrm{r}$).

The described properties also hint at the behavior of the images in the limiting cases, for sources at large or small angular separations $\beta$ from the lens, in comparison with its Einstein radius. For $\beta \gg \theta_\mathrm{E}$ the positive-parity image converges to the source position, $\boldsymbol{\theta}_+ \to \boldsymbol{\beta}$, and its magnification approaches unity, $1/|\det J(\boldsymbol{\theta}_+)| \to 1$. Hence, the positive-parity image merges with the true position and appearance of the source, as it would be seen in the absence of the lens. On the other hand, the negative-parity image shrinks, $1/|\det J(\boldsymbol{\theta}_-)| \to 0$, and its position converges to the lens position, $\theta_- \to 0$. The negative-parity image thus "disappears" at the lens position.

For $\beta \ll \theta_\mathrm{E}$, the positive-parity image approaches the Einstein radius from outside ($\boldsymbol{\theta}_+ \to \theta_\mathrm{E}\,\boldsymbol{\beta}/\beta$) and the negative-parity image approaches the Einstein radius from inside on the opposite side of the lens ($\boldsymbol{\theta}_- \to -\theta_\mathrm{E}\,\boldsymbol{\beta}/\beta$), as the magnifications of both diverge. Therefore, for a point-like source the images change discontinuously, from two opposite points for arbitrarily small but non-zero $\beta$, to the circle connecting them when the source is perfectly aligned behind the lens. This can be seen in the last two panels of Figure 3.2.

Setting the Jacobian from Equation (3.6) equal to zero, we get

$$|\boldsymbol{\theta}| = \theta_\mathrm{E}\,. \tag{3.7}$$

Hence, the critical curve of the point-mass lens is a circle with the Einstein radius, marked in blue in Figure 3.1 and Figure 3.2. The critical curve is identical with the image of a point source directly behind the lens in Equation (3.5). This implies that the caustic of the point-mass lens is the single point $\beta = 0$, which can be confirmed by substituting $\boldsymbol{\theta}$ from Equation (3.7) in the lens Equation (3.2).

In order to compute the point-source amplification for the point-mass lens, we use the Jacobian from Equation (3.6) in Equation (2.3),

$$A_0 = |\det J(\boldsymbol{\theta}_+)|^{-1} + |\det J(\boldsymbol{\theta}_-)|^{-1} = \left[1 - (\theta_\mathrm{E}/\theta_+)^4\right]^{-1} + \left[(\theta_\mathrm{E}/\theta_-)^4 - 1\right]^{-1} . \tag{3.8}$$

Substituting for $\boldsymbol{\theta}_+$ and $\boldsymbol{\theta}_-$ from Equation (3.4) yields

$$A_0(\boldsymbol{\beta}) = \frac{\beta^2 + 2\,\theta_\mathrm{E}^2}{\beta\,\sqrt{\beta^2 + 4\,\theta_\mathrm{E}^2}} , \tag{3.9}$$

a simple expression showing that the point-source amplification depends only on $\beta/\theta_\mathrm{E}$, the source position in units of the Einstein radius.

As shown by the black curve in Figure 3.3, with $\beta_\mathrm{c} = \beta$, the amplification given by Equation (3.9) is a monotonically decreasing function of $\beta/\theta_\mathrm{E}$. For a source positioned well outside the Einstein radius, $\beta \gg \theta_\mathrm{E}$,

$$A_0(\boldsymbol{\beta}) \approx 1 + 2\left(\frac{\beta}{\theta_\mathrm{E}}\right)^{-4} , \tag{3.10}$$

the point-source amplification decreases to unity, corresponding to an unamplified source flux. For a source positioned well inside the Einstein radius, $\beta \ll \theta_\mathrm{E}$,

$$A_0(\boldsymbol{\beta}) \approx \frac{\theta_\mathrm{E}}{\beta} + \frac{3\,\beta}{8\,\theta_\mathrm{E}} , \tag{3.11}$$

the point-source amplification reveals the divergence at the origin, i.e., for a point source perfectly aligned behind the point lens ($\beta = 0$).

## 3.3 Images of an Extended Source

As mentioned in Section 2.2, the non-physical divergence of the amplification $A_0$ is associated with the non-physical concept of a point source. For an extended source, each of its points has two images, as described above. The images of the points on the boundary of the source form the boundaries of the images, as illustrated in Figure 3.2 for a circular source with radius

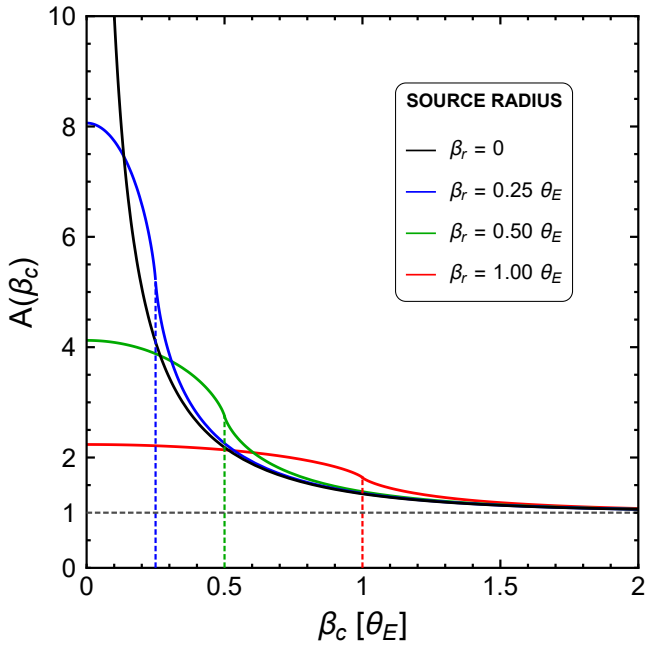


**Figure 3.3:** Amplification of flux from a source centered at position $\beta_c$ by a point-mass lens. Black curve: point-source amplification $A_0(\beta_c)$ given by Equation (3.9). Blue, green, and red curves: amplification $A(\beta_c)$ given by Equation (2.5) of a uniformly bright circular source with different radii $\beta_r$, as marked in the figure. To the left of the vertical dashed line of a particular color the lens caustic lies on the source of the corresponding radius.

$\beta_r = 0.25\,\theta_E$ at different positions $\beta_c$. The position of the source and its center is indicated by the pale red disk and a pale yellow dot, respectively. The positions of the images of the source and its center are marked by the bright red patches with bright yellow dots (or a bright yellow circle in the last panel). If the point-like caustic of the lens lies outside the boundary of the source (as in the first five panels of Figure 3.2), there are two separate images. If the caustic lies on the source (as in the last panel of Figure 3.2), the two images merge and form a ring-like image along the Einstein circle. In the sixth panel, the caustic lies exactly on the bottom edge of the source disk. This point at the edge is imaged onto the Einstein circle, and the outer (top) and inner (bottom) images of the source touch exactly at the two symmetric points lying at the intersection of the circle and the horizontal axis.

For a source with a surface-brightness distribution $I(\boldsymbol{\beta})$ the amplification is obtained from Equation (2.5), using the expression for the point-source amplification $A_0$ from Equation (3.9).

As described in Section 2.2, integration over the surface of the source eliminates the divergence and yields a finite value of the amplification. For illustration, Figure 3.3 includes the amplification as a function of source-center position $\beta_c$ for uniformly bright circular sources of three different radii $\beta_r \in \{0.25, 0.5, 1\}\,\theta_E$. An analytic expression for the amplification of such a source was derived by Witt & Mao (1994). As seen from the figure, smaller sources may achieve larger peak amplification, while for larger sources with $\beta_r > \theta_E$ the peak amplification drops to 1 and the influence of the lens becomes negligible. Note also that for sources positioned off the caustic, to the right of the corresponding vertical dashed lines in the figure ($\beta_c > \beta_r$), the amplification rapidly converges to the point-source amplification. Since the source is uniformly bright, the blue curve for $\beta_r = 0.25\,\theta_E$ shows the total magnification of the bright red images in Figure 3.2. For example, the Einstein ring in the last panel for $\beta_c = 0$ subtends a solid angle (has an area) about eight times larger than the source.

## 3.4 Point-mass-lens Convergence, Shear, and Phase

The lens potential for the point-mass lens can be obtained by combining the deflection angle in Equation (3.1) with the expression in Equation (2.6), yielding

$$\psi(\boldsymbol{\theta}) = \theta_E^2\, \ln|\,\boldsymbol{\theta}\,|\,. \tag{3.12}$$

The potential can be used to compute the point-mass-lens convergence from Equation (2.9),

$$\kappa(\boldsymbol{\theta}) = \pi\,\theta_E^2\,\delta(\boldsymbol{\theta})\,, \tag{3.13}$$

which is zero anywhere except at the position of the lens. The distortions of the images are thus given purely by the point-mass-lens shear. From Equation (2.10) we obtain

$$\gamma(\boldsymbol{\theta}) = \left(\frac{\theta_E}{\theta}\right)^2, \tag{3.14}$$

which is divergent at the lens position, equal to unity at the Einstein radius, and drops to zero for $\theta \gg \theta_E$.

The orientation of the image distortion is given by the phase $\varphi$, for which Equation (2.11) yields

$$[\,\cos 2\varphi(\boldsymbol{\theta}),\, \sin 2\varphi(\boldsymbol{\theta})\,] = \left[\frac{\theta_2^2 - \theta_1^2}{\theta^2}, -\frac{2\,\theta_1\,\theta_2}{\theta^2}\right]. \tag{3.15}$$

The interpretation of the phase can be found by introducing polar coordinates in the image plane, $[\theta_1, \theta_2] = \theta\,[\cos\phi, \sin\phi]$. Equation (3.15) then shows that $\varphi(\boldsymbol{\theta}) = \varphi(\phi) = \phi + \pi/2 + k\,\pi$, where $k$ is an integer included to obtain the phase in the preferred $\pi-$wide definition interval. This result shows that the images formed by a point-mass lens are always oriented tangentially, perpendicular to the position angle $\phi$.

# Chapter 4

## Microlensing By Stars and Planets in Our Galaxy

### 4.1 Microlensing by Single Stars

In spite of its simplicity, the point-mass lens described in detail in Chapter 3 is not a toy model. It provides an excellent description of gravitational lensing by compact massive astrophysical objects. The mass and size of such objects are constrained by the compactness criterion, which requires their angular size to be substantially smaller than their angular Einstein radius for background sources of interest. Such objects do not even require exact spherical symmetry, since their gravitational field is dominated at larger distances by the point-mass monopole term.

Distant stars and planets in our Galaxy fit the criterion perfectly. Hence, they may act as point-mass lenses for more distant background stars as sources. However, their Einstein radii are typically $\theta_{\rm E} \lesssim 10^{-3}$arcsec, too small for the images to be resolved observationally, as pointed out already by Einstein (1936). The only chance of detecting such lensing would be by measuring the total flux amplification of the source, but this would require knowing the intrinsic flux of the source. In addition, as argued by Einstein (1936), the chance of having a background star within an Einstein radius of the line of sight to a foreground star is very low.

Nevertheless, for stars in the Galaxy their relative proper motions are high enough for the source to cross the Einstein radius of the lens on a timescale of days to months Liebes (1964); Refsdal (1964); Paczyński (1986). Measuring the light curve of the source would then solve the first problem, by monitoring the gradual increase of its flux and decrease back to its intrinsic

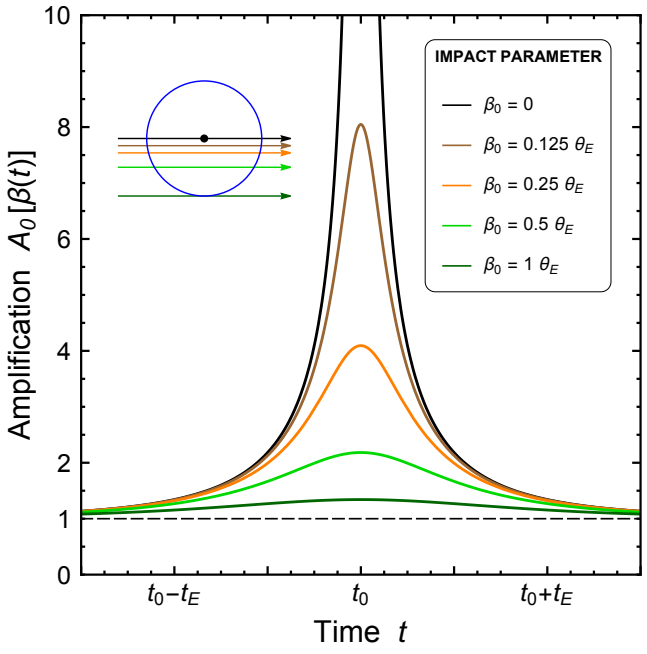


**Figure 4.1:** Microlensing light curves for a point source lensed by a point-mass lens. Point-source amplification $A_0$ is plotted as a function of time for five values of the impact parameter $\beta_0$ given in the inset at right. The source trajectories in the rest frame of the lens (marked by the black point and the blue Einstein circle) are indicated by the arrows in the inset at left. The peak time is denoted by $t_0$; the Einstein-radius crossing time by $t_\mathrm{E}$.

value, as the lens passes in the foreground. This scenario describes the effect known as Galactic gravitational microlensing. The term "microlensing" is generally used for lensing by stars and stellar or planetary systems in our own or any other galaxy. Even though the image separations are too small for them to be resolved, microlensing is manifested and can be detected by the changing amplification of background sources due to the relative source–lens proper motion.

The relative source–lens trajectory in the course of a typical microlensing event can be approximated by a straight-line segment. The angular source-lens separation as a function of time can then be expressed as

$$\beta(t) = \sqrt{\beta_0^2 + \left(\frac{t - t_0}{t_\mathrm{E}}\right)^2 \theta_\mathrm{E}^2}\,, \tag{4.1}$$

where $\beta_0$ is the impact parameter, $t_0$ is the closest-approach time, and $t_\mathrm{E}$ is the Einstein-radius crossing time. The light curve for a typical microlensing event is then given by $A_0[\beta(t)]$, substituting from Equation (4.1) in the point-source amplification formula from Equation (3.9).

Figure 4.1 includes examples of microlensing light curves for five values of the impact parameter $\beta_0$. The peak amplifications, $A_0(\beta_0)$, can also be read off the black curve in Figure 3.3. If the source just grazes the Einstein circle of the lens (dark green curve in Figure 4.1), the peak amplification is very well detectable but fairly low, $A_0(\theta_\mathrm{E}) = 3/\sqrt{5} \approx 1.34$. For lower impact parameters the source may achieve significant brightening at the peak of the event, $A_0 \gtrsim 8$ for $\beta_0 < 0.125\,\theta_\mathrm{E}$. The effect is thus strong enough to be detectable even by small telescopes under favorable conditions.

The feasibility of detecting microlensing thus depends on the frequency of configurations providing the required lens–source alignment. For a source star in the Magellanic Clouds or in the Galactic Bulge the probability that it lies within an Einstein radius of a foreground star was estimated by Paczyński (1986, 1991) to be on the order of $10^{-6}$. In other words, one in a million such stars should be lensed at any time. Monitoring millions of such stars over months or years should yield many detections of such microlensing events. The rich star fields in the mentioned regions are perfect targets for automated monitoring surveys, which may detect numerous microlensing events in real time.

The initial microlensing surveys such as MACHO (Alcock et al. 1997), OGLE (Udalski et al. 1997), EROS (Renault et al. 1997) or DUO (Alard & Guibert 1997) started in the early 1990's with the goal to detect microlensing by planetary- or stellar-mass compact dark-matter objects, so-called MACHOs (Massive Astrophysical Compact Halo Objects). However, analyses of the detected event statistics ruled out the hypothesis that the majority of dark matter occurs in the form of MACHOs (Tisserand et al. 2007). The observed microlensing events are compatible with the lenses being stars from Galactic stellar populations (Popowski et al. 2005; Sumi et al. 2006). The detection rate, which started at tens of events per year, has gradually increased up to thousands of events per year with the currently operating surveys, which include OGLE, MOA (Abe et al. 1997), and KMTNet (Kim et al. 2016).

Starting soon after the first surveys, microlensing follow-up projects such as PLANET (Albrow et al. 1998), $\mu$FUN (Gould et al. 2010), RoboNet (Tsapras et al. 2009), MiNDSTEp (Dominik et al. 2010), or ROME/REA (Tsapras et al. 2019) have been set up to measure the light curves of events detected by the surveys with better time coverage and photometry. The

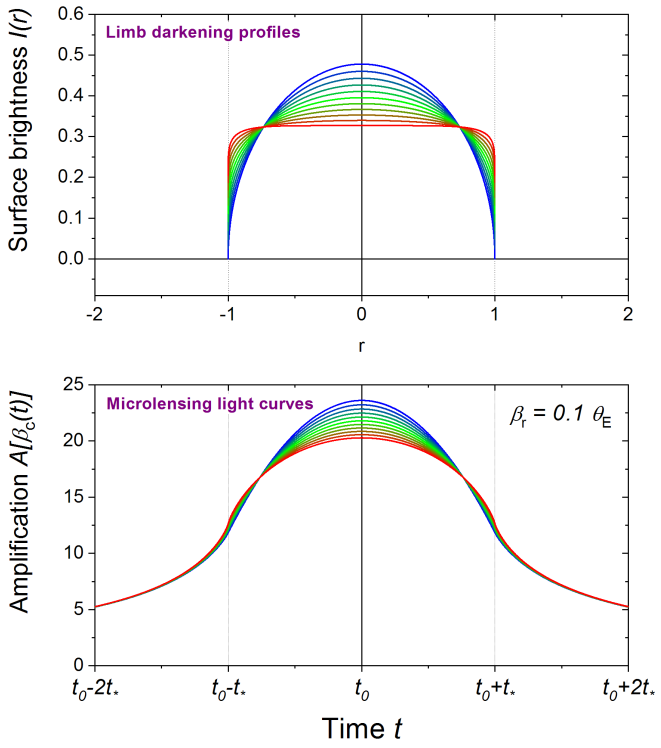


**Figure 4.2:** Microlensing light curves for an extended limb-darkened source lensed by a point-mass lens. Extended-source amplification $A$ is plotted in the bottom panel as a function of time for a circular source with radius $\beta_{\rm r} = 0.1\,\theta_{\rm E}$ passing behind the lens with a zero impact parameter. The different colors of the light curves correspond to different limb-darkening profiles $I(r)$ of the source shown in the top panel. The peak time is denoted by $t_0$; the source-radius crossing time by $t_*$. The dotted vertical lines are aligned to mark the source edges (top) and the times of their crossing (bottom).

goal of these projects has been the detection anomalous events with deviations from the simple point-source point-lens light curves seen in Figure 4.1. Such anomalies may arise from parallax effects due to deviations of relative source–lens–observer motions from uniform rectilinear motion, from extended-source effects when the lens caustic resolves the disk of the source star, or from the lens or source star being a component of a stellar system such as a binary star. However, the primary sought anomalies are those arising from the additional gravitational lensing effect of planets around the lens star, described here in Section 4.2.

For events with an impact parameter low enough to be comparable or lower than the angular radius of the source star $\beta_0 \lesssim \beta_{\rm r}$, extended-source effects become significant, limiting the peak

amplification. In terms of Einstein radii, source star radii in microlensing events are usually in the range $10^{-4}$–$10^{-2}\,\theta_{\rm E}$, though in exceptional cases they may be larger than $0.1\,\theta_{\rm E}$. Instead of point sources, such stars should be treated as circular sources (see Figure 3.2). However, stellar surface brightness distribution is not uniform, it follows a limb-darkened radial profile $I(r)$, where dimensionless $r$ runs from 0 at the disk center to 1 at its limb. The limb darkening depends sensitively on wavelength and on the stellar-atmosphere parameters of the source star. The main implication for microlensing is that the light-curve shape at the peak loses its achromaticity and depends on the photometric band used for observation. On the one hand, this is a complication for the event analysis. On the other hand, such events can be used for the unique measurement of the limb darkening of their source stars (Heyrovský 2003).

We illustrate the relation between the limb-darkening profile $I(r)$ and the shape of the light curve in Figure 4.2 on the example of a microlensing event with a source-star radius $\beta_{\rm r} = 0.1\,\theta_{\rm E}$ and a zero impact parameter. The light curves in the bottom panel are plotted with time marked in source-radius crossing times, $t_* = t_{\rm E}\,\beta_{\rm r}/\theta_{\rm E}$, and the position of the source center $\beta_{\rm c}(t)$ computed from Equation (4.1). The limb-darkening profiles, normalized in the top panel to unit flux, span the range of shapes obtained by a principal component analysis of stellar model-atmosphere profiles (Heyrovský 2003, 2008), with the flattest plotted in red and the most peaked profile plotted in blue. The correspondingly colored light curves in the bottom panel, which are computed using the respective $I(r)$ profiles in Equation (2.5), can be seen to trace the shape of the underlying limb-darkening profiles. As the lens caustic exits the source the differences rapidly vanish. At a separation of two source radii (edges of the bottom plot) the light curves regain their achromaticity and become indistinguishable.

This sensitivity of the microlensing light curves has been used in a number of events to measure the source-star limb darkening (e.g., Cassan et al. 2006; Fouqué et al. 2010; Choi et al. 2012). These caustic-crossing events can also reveal the possible presence of star spots on surface the source star (Heyrovský & Sasselov 2000). Spectroscopic monitoring during the crossing can reveal details of the structure of the star's atmosphere (Heyrovský et al. 2000).

## 4.2 Microlensing by Binary Stars and by Stars with a Planet

A large fraction of stars in the Galaxy are components of multiple stellar systems. In the mass range 0.1–0.5 $M_\odot$ at least 26%, and in the mass range 0.7–1.3 $M_\odot$ at least 44% of stars have at least one stellar companion (Duchêne & Kraus 2013). Similarly, based on the statistics of exoplanet detections, a majority of stars are expected to host at least one planet (Cassan et al. 2012; Gaudi 2021). Microlensing by such stars often cannot be described by the simple light-deflection formula in Equation (3.1). The presence of other bodies near the lens star can be expected to influence the observed light curves.

The simplest model that can describe lensing by a binary star or a star with a planet is the two-point-mass lens, explored in detail first by Schneider & Weiss (1986) for the equal-mass case and by Erdl & Schneider (1993) for the case of a general mass ratio. In the post-Newtonian approximation light deflection is additive, since it arises from the additive gravitational potential. For two point masses with projected lens-plane positions $\boldsymbol{\theta}_\mathrm{A}$, $\boldsymbol{\theta}_\mathrm{B}$ and masses $M_\mathrm{A}$, $M_\mathrm{B}$ the total deflection angle can be written as

$$\boldsymbol{\alpha}(\boldsymbol{\theta}) = \frac{4\,G\,M}{c^2\,D_\mathrm{l}} \left[ \mu_\mathrm{A} \frac{\boldsymbol{\theta} - \boldsymbol{\theta}_\mathrm{A}}{|\boldsymbol{\theta} - \boldsymbol{\theta}_\mathrm{A}|^2} + \mu_\mathrm{B} \frac{\boldsymbol{\theta} - \boldsymbol{\theta}_\mathrm{B}}{|\boldsymbol{\theta} - \boldsymbol{\theta}_\mathrm{B}|^2} \right] , \tag{4.2}$$

where $M = M_\mathrm{A} + M_\mathrm{B}$ is the total mass of the lens and $\{\mu_\mathrm{A}, \mu_\mathrm{B}\} = \{M_\mathrm{A}/M, M_\mathrm{B}/M\}$ are the fractional masses of the two components satisfying the relation $\mu_\mathrm{A} + \mu_\mathrm{B} = 1$.

Using the deflection angle from Equation (4.2) in Equation (2.1) yields the lens equation for the two-point-mass lens:

$$\boldsymbol{\beta} = \boldsymbol{\theta} - \theta_\mathrm{E}^2 \left[ \mu_\mathrm{A} \frac{\boldsymbol{\theta} - \boldsymbol{\theta}_\mathrm{A}}{|\boldsymbol{\theta} - \boldsymbol{\theta}_\mathrm{A}|^2} + \mu_\mathrm{B} \frac{\boldsymbol{\theta} - \boldsymbol{\theta}_\mathrm{B}}{|\boldsymbol{\theta} - \boldsymbol{\theta}_\mathrm{B}|^2} \right] , \tag{4.3}$$

where the Einstein radius $\theta_\mathrm{E}$ corresponds to the total mass of the lens $M$. In the notation introduced by Witt (1990) the vectorial quantities appearing in the equation can be replaced by complex numbers. The equation can then be converted to a fifth degree polynomial equation, which can be seen in Equation (6) in Appendix A with $n = 2$. For general positions and masses of the lens components, the lens equation thus cannot be inverted analytically and the image positions have to be computed numerically.

In principle, not all roots of the complex equation solve the lens equation, since the polynomial equation is not fully equivalent with Equation (4.3). The criterion for the number of

images is the position of the source $\boldsymbol{\beta}$ with respect to the lens caustic, which is formed by one or more closed curves instead of the single point in the case of the point-mass lens. For source positions lying outside the lens caustic two of the five roots of the complex polynomial equation are spurious; they do not solve Equation (4.3). Hence, such a source has only three images. For points in the source plane outside the caustic none of the roots are spurious and such points have five images.

The Jacobian of Equation (4.3) is

$$\det J(\boldsymbol{\theta}) = 1 - \theta_{\mathrm{E}}^4 \left[ \frac{\mu_{\mathrm{A}}}{|\boldsymbol{\theta} - \boldsymbol{\theta}_{\mathrm{A}}|^2} + \frac{\mu_{\mathrm{B}}}{|\boldsymbol{\theta} - \boldsymbol{\theta}_{\mathrm{B}}|^2} \right]^2 . \tag{4.4}$$

To obtain the point-source amplification for the two-point-mass lens, the values of the Jacobian in the three or five numerically computed images $\boldsymbol{\theta}_i$ have to be used in the general formula in Equation (2.3). The light-curve structure is substantially more complex than in the point-mass-lens case. For a general projected trajectory of the source in the source plane, the point-source-amplification increases as the source approaches the lens. However, closer to the lens the light curve is determined by the structure of the caustic of the lens, with the amplification sharply diverging at all points where the source crosses the caustic. Just as in the point-mass-lens case, close to these caustic crossings the point-source approximation has to be abandoned and the amplification has to be computed using Equation (2.5) with the source star modeled by a limb-darkened circular source. As shown by Pejcha & Heyrovský (2009), in the two-point-mass lens the regions of sensitivity to the non-zero angular size of the source star and its limb darkening generally extend much further than in the point-mass lens, especially outside the cusps of the caustic.

By setting the Jacobian from Equation (4.4) equal to zero we obtain the critical curve and, by mapping the critical-curve points back to the source plane using Equation (4.3), the caustic of the lens. The scale of these curves is given by the Einstein radius $\theta_{\mathrm{E}}$, their orientation by the axis of symmetry connecting the two points, and their location by the position of one of the points (or, alternatively, their center of mass or centroid). Their shape is given by the two remaining parameters contained in Equation (4.4): one of the fractional masses and the separation of the two points $s = |\boldsymbol{\theta}_{\mathrm{B}} - \boldsymbol{\theta}_{\mathrm{A}}|/\theta_{\mathrm{E}}$, expressed customarily in units of the Einstein radius. The structure of the critical curve and caustic is thus determined by the combination

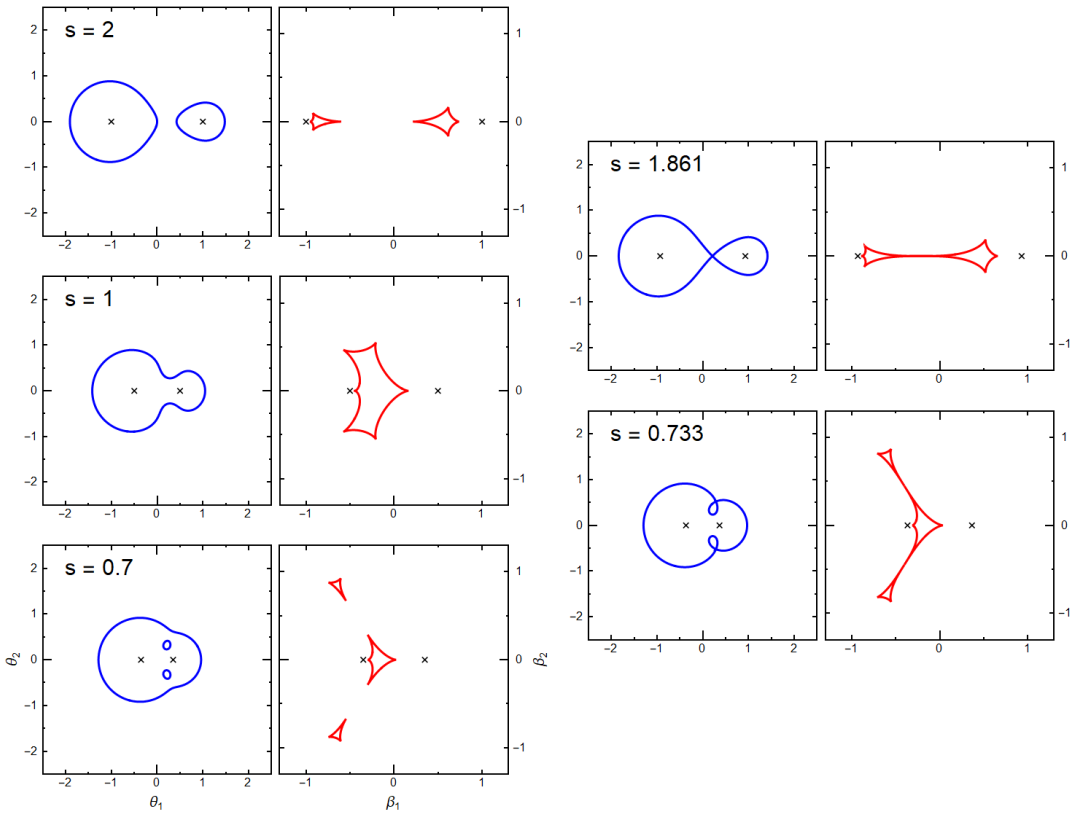


**Figure 4.3:** Critical curves and caustics for a two-point-mass lens with fractional masses $\{\mu_{\rm A}, \mu_{\rm B}\} = \{0.8, 0.2\}$ for five separations $s$ marked in the pairs of panels. Critical curves (blue) are plotted in the lens plane; caustics (red) are plotted in the source plane (note the different scales). The point-mass positions are marked by black crosses. Left column: examples of the wide, intermediate, and close regimes (from top). Right column: configurations at the boundaries between the regimes.

$\{\mu_{\rm A}, s\}$, which defines the parameter space of the lens.

As an example, we present in Figure 4.3 plots of the critical curves (blue) and caustics (red) for a two-point-mass lens with fractional masses $\{\mu_{\rm A}, \mu_{\rm B}\} = \{0.8, 0.2\}$ for five values of the separation $s$. In all cases the centroid of the lens is placed at the origin, the two lens components (marked by crosses) are positioned along the horizontal axis (the more massive A on the left), and the axes in the lens and source planes are marked in Einstein-radius units. The lens has three different regimes, defined by the topology of the critical curve and geometry of the caustic, usually named by the separation "wide", "intermediate" (or "resonant"), and

"close". The left column in Figure 4.3 illustrates typical cases for either regime.

In the wide regime (shown in the top pair of panels for $s = 2$), the critical curve consists of two loops around each of the components. The caustic has two corresponding loops, each with four sharp points (cusps), connected by smooth segments (folds). At larger separations $s$, the critical curve converges to two Einstein circles with radii $\sqrt{0.8}\,\theta_\mathrm{E}$ and $\sqrt{0.2}\,\theta_\mathrm{E}$, while the loops of the caustic shrink to points at the positions of the components. Such a configuration corresponds to two independent point-mass lenses with masses $M_\mathrm{A}$, $M_\mathrm{B}$.

In the intermediate regime (shown in the middle pair of panels for $s = 1$), the critical curve has one loop around both components and the corresponding single loop of the caustic has six cusps, with the two cusps along the horizontal axis lying between the components. In the close regime (shown in the bottom pair of panels for $s = 0.7$), the critical curve has one loop around both components and two additional small loops inside the first loop. The caustic has three loops: a central one with four cusps along the horizontal axis, an a symmetrically offset pair of small loops with three cusps each. At smaller separations $s$, the outer loop of the critical curve converges to an Einstein circle with radius $\theta_\mathrm{E}$ and the small inner loops shrink and approach the origin. The central loop of the caustic shrinks to a point at the origin, while the two off-axis loops recede asymptotically far from the origin. Such a configuration corresponds to a single point-mass lens with the total mass $M$.

The boundary cases between the three regimes are shown in the right column in Figure 4.3. At $s \approx 1.861$ the two loops of the critical curve come into contact at a point on the horizontal axis between the components. Viewed from larger separations, the two loops merge into one; viewed from smaller separations, the loops of the components detach from the common loop. The caustic undergoes a beak-to-beak metamorphosis, in which two facing cusps touch and disappear (here for smaller separations), reducing the total number of cusps on the caustic by two. At $s \approx 0.733$ the two lobes formed on the critical curve above and below the horizontal axis between the components pinch off and, for smaller separations, detach as separate loops inward. The caustic undergoes two simultaneous beak-to-beak metamorphoses, in which the two three-cusped loops present at smaller separations touch the off-axis cusps of the central loop, so that four cusps vanish for larger separations.

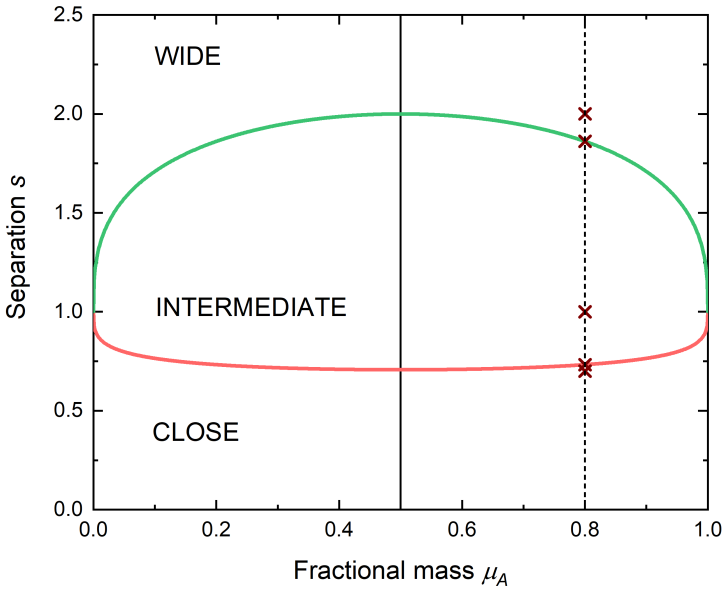


**Figure 4.4:** Lensing regimes in the parameter space of the two-point-mass lens, defined by the fractional mass $\mu_\mathrm{A}$ of one point and the separation $s$ of the points. The wide–intermediate boundary (green curve) is given by Equation (4.5); the close–intermediate boundary (pink curve) is given by Equation (4.6). The solid vertical line of symmetry at $\mu_\mathrm{A} = 0.5$ marks the equal-mass case. The dashed line at $\mu_\mathrm{A} = 0.8$ and the crosses along it mark the parameter combinations of the examples presented in Figure 4.3.

The same three regimes illustrated in Figure 4.3 for fractional mass $\mu_\mathrm{A} = 0.8$ occur for any other fractional mass. However, the boundaries between them in the parameter space of the lens depend on the value of $\mu_\mathrm{A}$. As shown by Erdl & Schneider (1993) and as demonstrated in Section 3.2 of Appendix B, the boundary between the wide and intermediate regimes occurs at separation

$$s_\mathrm{w} = \left[ \sqrt[3]{\mu_\mathrm{A}} + \sqrt[3]{1-\mu_\mathrm{A}} \right]^{3/2} , \tag{4.5}$$

and the boundary between the intermediate and close regimes occurs at separation

$$s_\mathrm{c} = \left[ \sqrt[3]{\mu_\mathrm{A}} + \sqrt[3]{1-\mu_\mathrm{A}} \right]^{-3/4} . \tag{4.6}$$

Both boundaries are plotted in the parameter space of the two-point-mass lens in Figure 4.4, with the positions of the five examples from Figure 4.3 marked by crosses along the dotted $\mu_\mathrm{A} = 0.8$ line. As seen from the figure, the intermediate regime always includes separation

$s = 1$ with the components exactly one Einstein radius apart. It is widest for the equal-mass case, where it reaches from $s = \sqrt{1/2}$ to $s = 2$, and shrinks from both sides to $s = 1$ for lenses in which the fractional mass of one of the components approaches zero. Most of the horizontal-axis range, for $0.03 \lesssim \mu_{\rm A} \lesssim 0.97$, corresponds to a binary-star lens (Jaroszyński et al. 2010), the left-most and right-most regions, $\mu_{\rm A} \lesssim 0.01$ and $\mu_{\rm A} \gtrsim 0.99$, correspond to a lens star with a planet.

Although the frequency of lens stars in binaries or multiple systems is expected to be high, in many configurations their microlensing light curves may be very similar to point-mass-lens light curves. Such configurations include primarily binaries with projected separations much lower or much higher than the Einstein radius. Nevertheless, Mao & Paczyński (1991) estimated that about 10% of microlensing events should strongly display the binary nature of the lens. The high number of detected binary-lens events is supported by results of the MACHO project (Alcock et al. 2000) and the OGLE project (Jaroszyński 2002; Jaroszyński et al. 2004, 2006; Skowron et al. 2007; Jaroszyński et al. 2010). The separations in these events peak around one Einstein radius and span the interval $s \in (0.3, 3.5)$ with an outlier at 7.454, which possibly involved a binary source rather than a binary lens (Alcock et al. 2000).

The extreme-mass-ratio limit of the two-point-mass lens model describes lensing by a star with a planet, which has been at the center of attention of the microlensing follow-up projects as mentioned in Section 4.1. For a planet in the intermediate regime and its nearest vicinity, its effect on the critical curve and caustic of the lens is the strongest. At larger or smaller separations the critical curve consists of a large Einstein circle and one or two tiny loops caused by the planet; all the corresponding loops of the caustic shrink rapidly as the separation moves away from one Einstein radius. Such planets stand a chance of being detected only if the source directly crosses one of the small caustic loops. Overall, microlensing is most sensitive to planets located at projected separations close to the Einstein radius of the host star.

The first planet found by gravitational microlensing was detected in event OGLE 2003-BLG-235 / MOA 2003-BLG-53 (Bond et al. 2004), with a fractional mass $\mu_{\rm A} \approx 0.0039$ and a separation $s \approx 1.12$. Hubble Space Telescope observations made 1.8 years after the peak of the event were used to detect light form the planetary-host lens star (Bennett et al. 2006). These

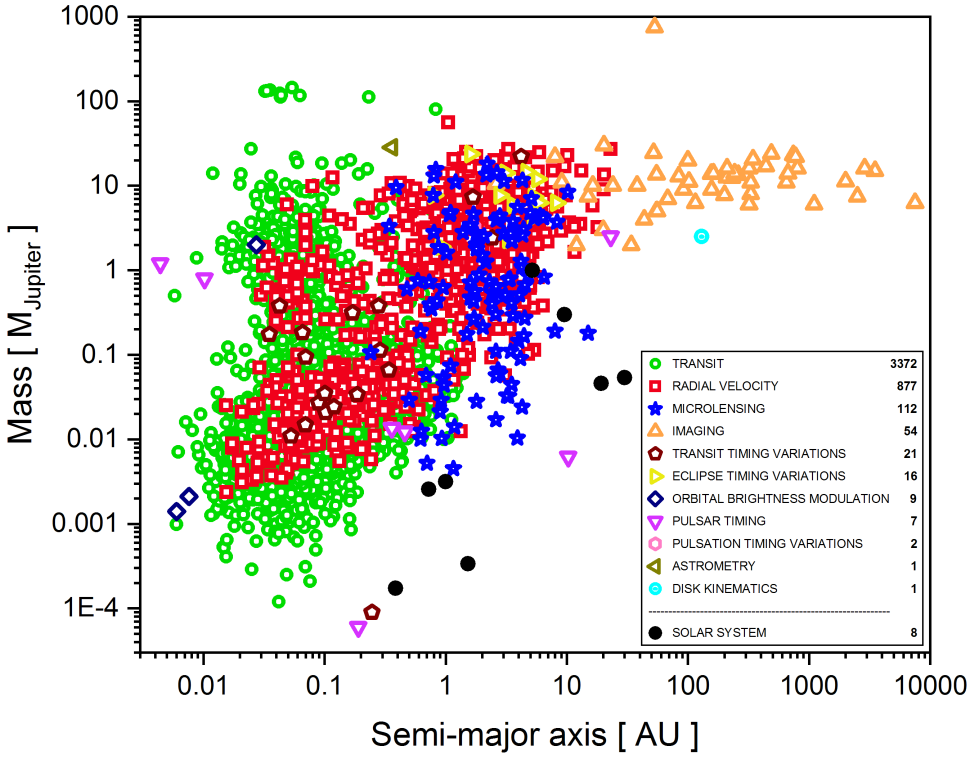


**Figure 4.5:** Confirmed planets included in the NASA Exoplanet Archive as of August 24, 2021, shown in a mass vs. semi-major axis scatter plot. Individual exoplanets are marked by color symbols corresponding to the method of their detection, listed in the legend together with the numbers of detections. Only planets with estimates of their mass and semi-major axis are illustrated. Black bullets marking the solar-system planets are included for orientation.

additional data show the lens consists of an $0.63\,M_\odot$ K-dwarf host star with an $2.6\,M_{\rm Jupiter}$ planet at a projected physical separation of 4.3 AU.

The third published planet detected by microlensing, found in event OGLE 2005-BLG-390 (Beaulieu et al. 2006), was more exciting due to its extremely low fractional mass $\mu_{\rm A} \approx 7.6 \times 10^{-5}$. Its fairly large separation $s \approx 1.6$ indicates that this wide-separation planet was detected because the source star directly crossed the small four-cusped caustic corresponding to the planet. In this event the lens consists of an $0.22\,M_\odot$ M-dwarf host star with a $5.5\,M_{\rm Earth}$ super-Earth planet at a projected physical separation of 2.6 AU. This event showed the main strengths of detecting planets by gravitational microlensing: sensitivity to low-mass planets due to the

slow decrease of the Einstein radius with mass ($\theta_{\rm E} \sim \sqrt{M}$), and sensitivity to planets at AU-scale separations from their host stars due to the lens-plane scale of the Einstein radius of a typical lens star toward the Galactic Bulge. The combination of these two strengths means that gravitational microlensing is ideally suited for detecting planets analogous to solar-system planets.

In Figure 4.5 we present an overview of the confirmed exoplanets plotted by their mass and semi-major axis, using data downloaded from the NASA Exoplanet Archive[1] on August 24, 2021. As of this date, a total of 4472 exoplanets had been detected by eleven different methods, 112 of them by microlensing. The detection methods are indicated by the color symbols; they are listed in the figure legend together with the numbers of detected planets. Of the total number, only the 4305 planets with provided estimates of mass and semi-major axis are included in the plot.

The different techniques are sensitive to different types of planets: transit surveys are primarily sensitive to planets in close-in orbits; radial velocity surveys primarily to massive planets and lower-mass planets in close-in orbits; imaging detections are sensitive to large (i.e., generally massive) planets in wide orbits. The distribution of the 111 blue-star symbols shows that microlensing surveys have led to the discovery of planets with masses as low as $1.4\,M_{\rm Earth}$ orbiting their host stars at distances from 0.2 to 20 AU. The main weaknesses of exoplanet discovery by microlensing are the one-time nature of the detection and the inability to study the atmosphere of the planet, due to the deflected light passing too far from the planet.

Nevertheless, by the growing statistics of discovered planets the technique will help expand our understanding of exoplanets in parameter-space regions that are difficult to reach by other methods. Of particular importance is the planned microlensing-based Galactic Exoplanet Survey (Penny et al. 2019), one of the core missions of the upcoming (Nancy Grace) Roman Space Telescope (formerly WFIRST, Spergel et al. 2015). This space-based survey is expected to detect $\sim$ 1400 bound exoplanets, with $\sim$ 200 of them having masses $\lesssim 3\,M_{\rm Earth}$. The detections may include not only exo-Earths, but also exo-Venuses, exo-Marses, and possibly even $\sim 0.02\,M_{\rm Earth}$ Ganymede-mass exoplanets (Penny et al. 2019). In addition, the survey will

[1] https://exoplanetarchive.ipac.caltech.edu/

be sensitive to free-floating planetary-mass objects and it is expected to place substantially improved upper limits on their population (Johnson et al. 2020).

## 4.3 Microlensing by Three-body Lenses

The microlensing-detected planets illustrated in Figure 4.5 include also several planets found as components of three-body lenses. The simplest example of such lens systems are stars hosting two planets. The first detected triple-lens microlensing event, OGLE-2006-BLG-109 (Gaudi et al. 2008; Bennett et al. 2010), involved a $0.5\,M_{\odot}$ star with a $0.73\,M_{\rm Jupiter}$ planet at 2.3 AU and a $0.27\,M_{\rm Jupiter}$ planet at 4.5 AU, similar to a scaled-down version of the Sun–Jupiter–Saturn system. Three more events with the lens formed by a star with two planets have been included in the NASA Exoplanet Archive since then: OGLE-2012-BLG-0026 (Han et al. 2013; Beaulieu et al. 2016), OGLE-2014-BLG-1722 (Suzuki et al. 2018), and OGLE-2018-BLG-1011 (Han et al. 2019).

The detected triple-lens events also include seven cases, in which the lens is formed by a binary star with a planet. In two of these events the planet orbits one of the binary components: OGLE-2008-BLG-092 (Poleski et al. 2014) and OGLE-2013-BLG-0341 (Gould et al. 2014). One event involves a circum-binary planet: OGLE-2007-BLG-349 (Bennett et al. 2016). In the remaining four events the projected configuration does not clearly indicate whether the planet orbits the binary or one of its components: OGLE-2016-BLG-0613 (Han et al. 2017), OGLE-2018-BLG-1700 (Han et al. 2020), OGLE-2006-BLG-284 (Bennett et al. 2020), and KMT-2019-BLG-1715 (Han et al. 2021).

In addition to stars with two planets and binary stars with a planet, possible three-body lenses include two other types of systems as yet undetected by microlensing: triple stars, and stars with a planet with a moon. The discovery of the latter would be particularly interesting, since no moon orbiting an exoplanet has been convincingly detected yet by any method. For triple-star systems to be detectable by microlensing, their projected positions would have to be not more than a few Einstein radii apart. Close-in triple systems with components a few *AU* apart would likely have serious problems with stability. A more likely scenario could involve a binary star with a distant companion fortuitously located close to the line of sight, so that

its projected position would lie within a few Einstein radii of the binary. Such configurations might occur, but their probability would be suppressed by the required geometric alignment.

Microlensing events involving a star+planet+moon lens (Han & Han 2002) should be geometrically more probable than those involving triple-star lenses. Nevertheless, in most cases any feature due to the moon would be weak and highly localized on the light curve (Han 2008), so that its detection would require excellent photometry and an excellent sampling rate (cadence) of observations. As shown by Liebig & Wambsganss (2010), detection would be more likely for dwarf source stars which cause less smearing of the features by the extended-source effect. The upcoming Galactic Exoplanet Survey by the Roman Space Telescope (Penny et al. 2019) might provide the best chance for exo-moon detection by microlensing.

For describing such microlensing events, all of the mentioned three-body systems can be modeled by the three-point-mass lens (or triple lens for short). Computing even point-source light curves for the triple lens is demanding, since it may produce $4, 6, 8$, or 10 images depending on the position of the source with respect to the caustic (Rhie 2003; Khavinson & Neumann 2006). The analysis and modeling of these events is hindered by the lack of insight into the general structure of critical curves and caustics of the lens. In the case of two-point-mass lenses, the analysis of events is greatly simplified by the understanding of the different regimes of the lens (shown in Figure 4.3), and by the knowledge of the boundaries separating these regimes in the parameter space of the lens (shown in Figure 4.4). There is no equivalent of Figure 4.3 and Figure 4.4 for the triple lens. A full overview of the different regimes of the general triple lens has not been published yet, not to mention their parameter-space boundaries. The main goal of the first three original papers presented in the appendix part of this thesis was to tackle this outstanding problem.

The general configuration of a triple lens is described by the projected positions of the three points in the lens plane and by their three masses, nine parameters in all. The total mass defines the Einstein radius, which can be used as a unit in the lens plane, leaving two of the fractional masses as free parameters. The geometry of the critical curve and caustic is independent of the location of the origin of the lens plane and of the orientation of its coordinate axes. By setting the origin (typically at the centroid, at the center of mass, or at one of the points) and by setting

the orientation (typically with two of the points aligned parallel with the horizontal axis) the six coordinates of the points are reduced to three free parameters. The parameter space for exploring the critical curves and caustics of the triple lens is five-dimensional: two parameters describe the combination of masses, and three parameters describe the spatial configuration of the points (i.e., the projected triangle spanned by them).

The need to explore a five-dimensional instead of a two-dimensional parameter space is one of the differences that raise triple-lens investigations above the studies of the simpler two-point-mass lens. In addition, triple-lens caustics are substantially more complex than those of the two-point-mass lens. The number of cusps on the caustic may change in swallow-tail or butterfly metamorphoses without any change occurring on the critical curve. Caustic loops corresponding to independent critical-curve loops may cross and overlap each other, and individual loops of the caustic may exhibit self-intersections. Finally, the triple lens does not have unique wide and close regimes. Certain configurations exhibit atypical caustics in the wide limit, and others exhibit atypical caustics or critical curves in the close limit (Daněk & Heyrovský 2015b).

## 4.4 Included Papers on Triple Lenses

In the first included paper (Daněk & Heyrovský 2015a, Appendix A) we develop tools useful for the exploration of properties of general $n-$point-mass lenses. First, we show that any contour of the Jacobian is equal to the critical curve of an appropriately re-scaled configuration of the lens. Negative contours correspond to critical curves of a lens with the points placed wider apart; positive contours to critical curves of a lens with the points placed closer together. The full set of Jacobian contours then illustrates the full range of critical curves of lens configurations with the same shape, from the close to the wide limit (as illustrated for the $\mu_{\mathrm{A}} = 0.8$ two-point-mass lens in Figure 1 of Appendix A). Next, we introduce the cusp curve, which intersects the Jacobian contours (i.e., re-scaled critical curves) at the positions of critical cusp images. This permits the study and visualization of the cusp numbers on the loops of the caustic in the image plane of the lens. Finally, we introduce the morph curve, which intersects the cusp curve at points corresponding to caustic metamorphoses. These points identify the configurations at which the cusp number (and thus the caustic geometry) changes. These tools are illustrated

on the example of a two-point-mass lens with beak-to-beak metamorphoses in Figure 2, and on the examples of a triple-lens configuration with beak-to-beak and swallow-tail (Figure 3) or butterfly (Figure 4) metamorphoses.

In the second included paper (Daněk & Heyrovský 2015b, Appendix B) we performed a detailed analysis of the critical curves and caustics of four two-parameter triple-lens models: a linear symmetric configuration of two equal masses with a variable third mass at the center, a linear asymmetric configuration of equal masses with a variable position of the central mass, an equilateral triangle configuration with two equal masses and a variable third mass, and an isosceles triangle configuration with equal masses and a variable vertex angle. For each of these models we derived parameter-space boundaries of the different lens regimes analogous to those in Figure 4.4 for the two-point-mass lens, including additional boundaries due to changing cusp numbers. Altogether we identified nine different topologies of the critical curve (defined by the number and mutual positions of its loops) as listed in Table 1, and 32 different structures of the caustic (defined by the number of loops and the numbers of cusps on them) as listed in Table 2. The isosceles model was found to be the richest: the computed boundaries divide its parameter space into twelve regions by critical-curve topology (corresponding to all nine topologies), and into 41 regions by caustic structure (corresponding to 28 different structures). Lens configurations with anomalous wide or close limits are illustrated and explained using cusp and morph curves in Jacobian contour plots.

In the third included paper (Daněk & Heyrovský 2019, Appendix C) we present a method for mapping the lens regimes with different critical-curve topologies for a lens with an arbitrary spatial configuration of three fixed masses. We parameterized the general triangular configuration of such a lens using the perimeter to define the size, and two fractional side lengths to define the shape. Plotting the latter two in a ternary diagram (shown in Figure 1) and adding the perimeter as the third parameter perpendicular to the diagram led to our representation of the parameter space as a ternary prism (Figure 2). For a given shape of the configuration we computed the six perimeter values at which its critical-curve topology changes by the identifying the contours passing through the six Jacobian saddle points. Plotted for a dense grid of different shapes, these six vertical points trace six surfaces that define the topology

boundaries in the three-dimensional parameter space. The result for three equal masses is plotted in Figure 3, and the topologies in the different regions are identified on a sequence of its horizontal sections shown in Figure 6. The full set consists of the same nine topologies found in Daněk & Heyrovský 2015b. Their probability of occurrence as a function of the perimeter of the configuration (in Einstein radius units) is shown in Figure 7 and Table 1. The paper includes similar analyses for two other combinations of masses: an equal-mass binary with a planet $10^4\times$ lighter than the binary; and a hierarchical star-planet-moon combination (masses in a $1 : 0.01 : 0.0001$ ratio). For both of these models we found two previously unknown topologies involving doubly-nested critical-curve loops (illustrated in Figure 16), bringing the current total number of identified triple-lens critical-curve topologies to eleven. The schematic topology line-up is shown in Figure 9 in order of appearance with increasing perimeter in the planet-in-binary model.

# Chapter 5

# Lensing By Galaxies

## 5.1 Galaxies as Gravitational Lenses

While gravitational lensing by individual stars is conceptually the simplest, lensing by galaxies and galaxy clusters is more widely known, largely due to its visual appeal. Due to their large Einstein radii, the multiple images formed by them of background sources typically have sufficient separations and sizes for their often spectacular configurations to be directly observed and imaged. Historically, galaxies were the first astrophysical objects for which gravitational lensing was detected. The discovery of the twin images of quasar Q0957+561 by Walsh et al. (1979) followed by the discovery of the foreground lens galaxy by Young et al. (1980) and Stockton (1980) provided the first convincing case of the effect predicted by Einstein (1936) and Zwicky (1937). Since the first discovery, hundreds of galaxy-scale gravitational lenses have been found and upcoming large-scale imaging surveys are expected to increase the number by several orders of magnitude (Metcalf et al. 2019).

Galaxies may contain up to $10^{12}$ stars, which precludes modeling their lensing by a system of point-mass lenses. Moreover, their mass is generally dominated by dark matter in a galactic halo, and includes also gas and dust. To describe the multiple imaging of background quasars or galaxies, the galaxy has to be thus modeled by a continuous mass distribution. This corresponds to the regime of strong lensing, described in Section 5.2.

Nevertheless, even individual stars in the lens galaxy may have an additional effect on the images of compact sources such as quasars. If the light of a particular image passes directly

through the region populated by stars of the galaxy, the relative motion of the source with respect to the fine caustic network formed by the stars may lead to a temporal modulation of the brightness of the image. This effect of quasar microlensing is described in Section 5.3.

## 5.2 Strong Lensing

In the thin-lens approximation discussed in Section 2.1, the distribution of matter in the lens galaxy can be represented by its column density, obtained by integrating its density along the line of sight. The result can be treated as a surface density $\Sigma(\boldsymbol{\theta})$ as a function of position in the lens plane. The light-deflection angle can be obtained by linear superposition of deflections from all points contributing to the surface density. In an analogy to the combination of two points masses in Equation (4.2), we get

$$\boldsymbol{\alpha}(\boldsymbol{\theta}) = \frac{4\,G\,D_\mathrm{l}}{c^2} \int \Sigma(\boldsymbol{\theta'})\,\frac{\boldsymbol{\theta}-\boldsymbol{\theta'}}{|\boldsymbol{\theta}-\boldsymbol{\theta'}|^2}\,\mathrm{d}^2\boldsymbol{\theta'}\,, \tag{5.1}$$

where the integral is performed over the mass distribution of the lens. For a general lens the light-deflection angle is not obtained from a simple analytic formula; it has to be computed by numerical integration for any lens-plane point $\boldsymbol{\theta}$ of interest.

The surface density is usually expressed in units of the critical surface density

$$\Sigma_\mathrm{cr} = \frac{c^2}{4\pi G}\,\frac{D_\mathrm{s}}{D_\mathrm{l}\,D_\mathrm{ls}}\,. \tag{5.2}$$

This peculiar combination of distances and constants corresponds for example to the surface density obtained by dividing the mass of an object by the area of the Einstein circle of a corresponding point mass, $\Sigma_\mathrm{cr} = M/(\pi\,D_\mathrm{l}^2\,\theta_\mathrm{E}^2)$. As illustrated below, the dimensionless surface density is the convergence of the lens,

$$\kappa(\boldsymbol{\theta}) = \frac{\Sigma(\boldsymbol{\theta})}{\Sigma_\mathrm{cr}}\,, \tag{5.3}$$

and the deflection angle can be expressed in its terms as

$$\boldsymbol{\alpha}(\boldsymbol{\theta}) = \frac{D_\mathrm{s}}{\pi\,D_\mathrm{ls}} \int \kappa(\boldsymbol{\theta'})\,\frac{\boldsymbol{\theta}-\boldsymbol{\theta'}}{|\boldsymbol{\theta}-\boldsymbol{\theta'}|^2}\,\mathrm{d}^2\boldsymbol{\theta'}\,. \tag{5.4}$$

A comparison of this expression with Equation (2.6) shows that the deflection corresponds to the lens potential

$$\psi(\boldsymbol{\theta}) = \frac{1}{\pi} \int \kappa(\boldsymbol{\theta'})\,\ln|\boldsymbol{\theta}-\boldsymbol{\theta'}|\,\mathrm{d}^2\boldsymbol{\theta'}\,, \tag{5.5}$$

which also corresponds to a linear combination of point-mass potentials from Equation (3.12). The expression in Equation (5.5) shows that the lens potential is the solution of the two-dimensional Poisson equation

$$\Delta_{\boldsymbol{\theta}}\,\psi(\boldsymbol{\theta}) = 2\,\kappa(\boldsymbol{\theta})\,. \tag{5.6}$$

This result also demonstrates that the convergence defined by Equation (5.3) satisfies the definition from Equation (2.9) as well. The lens equation can be written in terms of the lens potential using Equation (2.7).

For illustration, we present here an example of strong lensing by a galaxy using a cored pseudo-isothermal elliptical mass distribution (Kassiola & Kovner 1993; Keeton & Kochanek 1998), described by its convergence

$$\kappa(\boldsymbol{\theta}) = \frac{\kappa_0}{\sqrt{1+q^2\theta_1^2+\theta_2^2}}\,, \tag{5.7}$$

where the $\theta_1$ axis is aligned with the major axis of the distribution, $q \in [0,1]$ is the projected axis ratio, the lens-plane position $\boldsymbol{\theta}$ is expressed in units of the softening core scale $\theta_\mathrm{s}$, and $\kappa_0$ is the convergence at the center of the mass distribution. In terms of the parameters used by Keeton & Kochanek (1998), $\theta_\mathrm{s} = q\,s$ and $\kappa_0 = b_I/(2\,q\,s)$.

The components of the light-deflection angle for this model expressed in units of $\theta_\mathrm{s}$ are

$$\begin{aligned}
\alpha_1(\boldsymbol{\theta}) &= \frac{2\,D_\mathrm{s}\,\kappa_0}{D_\mathrm{ls}\,\sqrt{1-q^2}}\,\arctan\left[\frac{q\sqrt{1-q^2}\,\theta_1}{1+q\sqrt{1+q^2\theta_1^2+\theta_2^2}}\right] \\
\alpha_2(\boldsymbol{\theta}) &= \frac{2\,D_\mathrm{s}\,\kappa_0}{D_\mathrm{ls}\,\sqrt{1-q^2}}\,\operatorname{arctanh}\left[\frac{\sqrt{1-q^2}\,\theta_2}{q+\sqrt{1+q^2\theta_1^2+\theta_2^2}}\right]
\end{aligned}\,, \tag{5.8}$$

and the Jacobian is given by

$$\det J(\boldsymbol{\theta}) = 1 - \frac{2\,\kappa_0}{\sqrt{1+q^2\theta_1^2+\theta_2^2}} + \frac{4\,q\,\kappa_0^2}{\sqrt{1+q^2\theta_1^2+\theta_2^2}\left[\left(1+q\sqrt{1+q^2\theta_1^2+\theta_2^2}\right)^2 + q^2(1-q^2)\,\theta_1^2\right]}\,, \tag{5.9}$$

as derived by Keeton & Kochanek (1998).

Figure 5.1 shows an example of the two-component critical curve (left panel) and caustic (right panel) of the lens for parameters $\kappa_0 = 10$ and $q = 0.7$. The positions of two circular sources are indicated in the right panel. Both are centered at the same position, with the light-orange source being ten times larger than the dark-orange source. The images of the

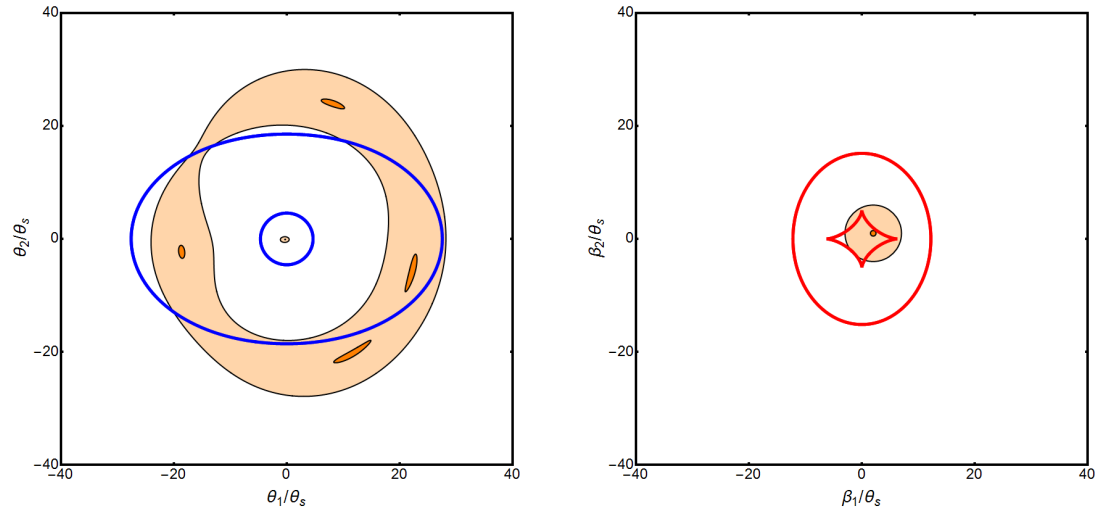


**Figure 5.1:** Strong lensing by a galaxy with an elliptical mass distribution of a small and a large source. The mass distribution given by Equation (5.7) has central convergence $\kappa_0 = 10$ and axis ratio $q = 0.7$, the lens-plane (left) and source-plane (right) axes are plotted in units of softening core scale $\theta_s$. Right panel: caustic (red) and two circular sources centered at $(\beta_1, \beta_2) = (2, 1)$, with radii 0.5 (dark orange) and 5 (light orange). Left panel: critical curve (blue) and images of the two sources shown in corresponding colors.

sources formed by the lens are shown in the left panel. The smaller source, which lies inside the inner four-cusped caustic, has five images including a tiny one inside the inner critical curve. For such a small source not lying directly on the caustic, all images are separated so that the number of macro-images is the same as the number of images for any part of the source. In the case of the larger source, which covers two cusps of the inner caustic and crosses its opposite fold, the situation is markedly different. Parts of the source inside the inner caustic have five images each, while those lying outside have only three images each. Overall, this source has two macro-images: a tiny one inside the inner critical curve, and a large ring-like image forming an equivalent of the point-mass-lens Einstein ring illustrated in the last panel of Figure 3.2.

The two source sizes were selected to illustrate the difference between galaxy-quasar and galaxy-galaxy lensing. The angular size of the bright emitting region of the quasar is typically much smaller than the angular size of the caustic components. Lensed quasars may thus form well separated multiple images and their amplification can often be approximated by the point-

source amplification. Angular sizes of lensed galaxies are often comparable or even larger than the sizes of caustic components. Very often two or more partial images are joined into a single macro-image, which may form large ring-like images such as the example shown in Figure 5.1. The amplification of such images cannot be approximated by the point-source amplification, it has to be evaluated using Equation (2.5).

## 5.3 Quasar Microlensing

The regime of quasar microlensing (Schmidt & Wambsganss 2010) is driven by secondary light deflection due to stars of the lens galaxy lying in the vicinity of a particular macro-image of the quasar source (such as one of the dark-orange images in the left panel of Figure 5.1). The relative proper motions of lensed quasars are sufficiently high for them to cross the caustics formed by the stars on timescales of weeks to months. If the size of the emitting region of the quasar is smaller than the characteristic structure scale of the caustic network, this motion may cause substantial brightness variations detectable in the light curve of the macro-image.

The situation can be modeled adequately by computing the light deflection due to all stars within a certain distance of the image position, in combination with the deflection due to a constant convergence, shear, and phase. These describe the local influence of all continuous matter plus all more distant stars. Using this model, the lens equation can written as

$$\boldsymbol{\beta} = \begin{pmatrix} 1-\kappa-\gamma\cos 2\varphi & -\gamma\sin 2\varphi \\ -\gamma\sin 2\varphi & 1-\kappa+\gamma\cos 2\varphi \end{pmatrix} \boldsymbol{\theta} - \widehat{\theta_{\mathrm{E}}}^2 \sum_i \frac{M_i}{\widehat{M}} \frac{\boldsymbol{\theta}-\boldsymbol{\theta_i}}{|\boldsymbol{\theta}-\boldsymbol{\theta_i}|^2}\,, \tag{5.10}$$

where constants $\kappa, \gamma$, and $\phi$ are the local convergence, shear, and phase, respectively. The summation includes all nearby stars with masses $M_i$ and positions $\boldsymbol{\theta_i}$, and $\widehat{\theta_{\mathrm{E}}}$ is the Einstein radius corresponding to mean stellar mass $\widehat{M}$. The local axis orientation is often chosen with the horizontal axis parallel to the phase, so that $\varphi = 0$.

The lens equation is generally not used for finding individual micro-images of the source. Instead, it is used for constructing an amplification map in the source plane by inverse ray shooting (Kayser et al. 1986), as mentioned in Section 2.2. With sufficiently small pixels for collecting the rays in the source plane, the obtained map yields a good approximation of the point-source amplification map, $A_0(\boldsymbol{\beta})$. For any size and brightness distribution $I(\boldsymbol{\beta})$ of the

quasar source, the amplification can be obtained by convolving the point-source amplification map with $I(\boldsymbol{\beta})$, as indicated by the first part of Equation (2.5). Wambsganss et al. (1992) and Wambsganss (1999) describe examples of efficient numerical methods based on inverse ray shooting.

In the top panel of Figure 5.2 we show an example of a quasar microlensing point-source amplification map $A_0(\boldsymbol{\beta})$ for a stellar population in a random distribution corresponding to convergence $\kappa_* = 0.3$. As seen in the color bar, black corresponds to unit amplification and the caustics can be seen as the yellowish boundaries of the higher-amplification regions. In this simple example, the external convergence and shear are neglected and all stars have the same mass. The source-plane axes are marked in stellar Einstein radii, which are typically $\sim 10^{-6}$arcsec for lens-galaxy stars.

The red dashed line indicates a sample trajectory of the source center, for which light curves are shown in the bottom panel. Four different uniform sources are illustrated to scale at top right: a point-like source, a small elliptical source, a large elliptical source (an inclined quasar disk), and a large circular source (the same disk in a face-on orientation). The corresponding light curves show a decreasing amplitude of their variations with source size, highest for the point-like source and lowest for the large sources. The light curves can be seen to be sensitive to the size and geometry of the source. Individual caustic crossings and approaches can be studied in the figure, for example, the first light-curve feature (a cusp approach) is not very sensitive to the differences between the sources, while the last feature (a cusp crossing) shows high sensitivity to source size. Not illustrated here, the caustic crossings are also shaped by the surface brightness distribution of the source, just as caustic crossings in microlensing events in our Galaxy follow the limb darkening of the source star (as shown in Figure 4.2).

The analyses of quasar microlensing observations have led to a number of unique measurements of properties of the quasar source. Some of the best results were obtained for quasar QSO 2237+0305, the quadruply imaged source in the "Einstein Cross" gravitational lens. Eigenbrod et al. (2008) used data from photometric and spectroscopic monitoring of the images to measure the size of the UV-continuum-emitting region of the quasar accretion disk as a function of wavelength, with results showing agreement with theoretical expectations for emission from a

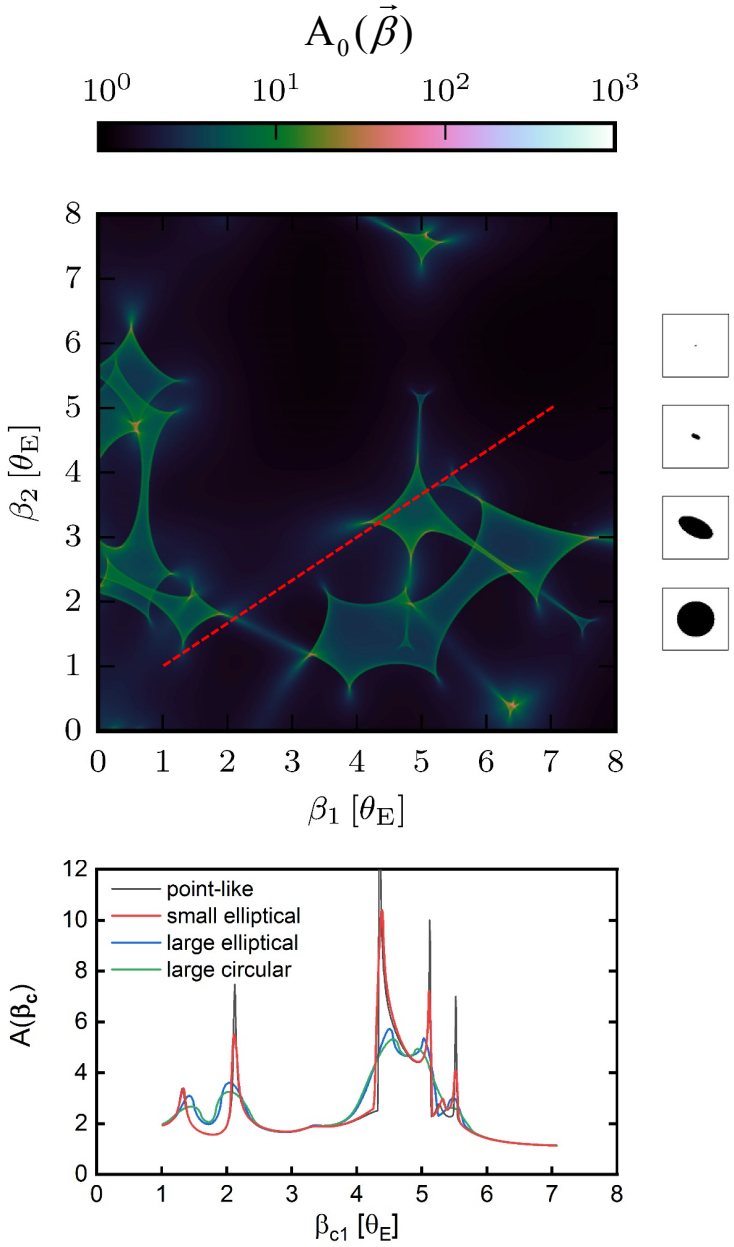


**Figure 5.2:** Quasar microlensing. Top: point-source amplification map $A_0(\boldsymbol{\beta})$ with source-center trajectory (red dashed line); projections of different quasar sources are shown at the right side. Bottom: quasar microlensing light curves (plotted here as a function of horizontal source-center position) for the four sources moving along the same trajectory. Horizontal axes of both panels are aligned for better correspondence of the light curves in the bottom panel with source position in the top panel.

thin accretion disk. For the same system, Sluse et al. (2011) used spectrophotometric data for two carbon emission lines to measure the size of the broad line region of the quasar.

In quasar accretion disks, higher energy emission generally arises from more compact regions,

with the hardest X-rays emitted from the innermost parts of the disk in the vicinity of the central black hole. X-rays should thus achieve highest microlensing variability, due to the small angular size of their emitting region which can lead to significant amplification even in high-density caustic networks. For six gravitationally lensed quasars monitored using the Chandra X-ray Observatory, Chen et al. (2012) detected microlensing in all of them. They also found strong iron K$\alpha$ emission in all of them, indicating that the line is emitted from a more compact region than the X-ray continuum. In another gravitationally lensed quasar, RX J1131-1231, monitoring by Chartas et al. (2012) revealed changes in the measured Fe K$\alpha$ line profile in the course of a microlensing caustic crossing. In this event the caustic resolved the emitting region in the inner disk of the quasar near the central black hole, where the line profile is dominated by strong-gravity effects. Quasar microlensing thus also provides a unique opportunity to resolve the innermost emitting region and test theoretical models of its structure.

## 5.4 Included Paper on Quasar Microlensing

In the fourth included paper (Ledvina et al. 2018, Appendix D) we studied microlensing of the Fe K$\alpha$ line theoretically, using a fully relativistic model of emission from an inclined thin accretion disk in the equatorial plane of a Kerr black hole. For simplicity, we used a maximally rotating Kerr black hole, for which the horizon coincides with the innermost stable circular orbit (ISCO). Due to the small size of the emitting region, we studied a single caustic crossing of the quasar disk by a linear fold caustic instead of using a simulated caustic network. We demonstrated new spectral features appearing in the line profile, shifting in energy and eventually disappearing in the course of the crossing. We explained the emergence of these features in terms of the location of the caustic with respect to constant energy-shift contours on the inclined disk (or, more exactly, on its asymptotic projection in the observer's plane of the sky). New peaks occur at energies with contours tangent from the inner side of the caustic, while new step-function edges occur at energies with contours tangent from the outer side of the caustic. We used an analytical model to derive the shape of these spectral features. Observed sequences of X-ray line-profiles can thus be used to constrain the geometry and physics of the innermost accretion disk.

# Chapter 6

## Lensing By Clusters of Galaxies

### 6.1 Galaxy Clusters as Gravitational Lenses

Galaxy clusters and superclusters are the largest gravitationally bound astrophysical objects that have formed by the current epoch in the history of the universe. Although rich clusters may contain up to thousands of galaxies, these constitute only a small fraction of their total mass. In the galaxy-cluster mass budget galaxies come in third (at $\sim 5\%$ of the total mass) after the dominant dark matter halo ($\sim 85\%$) and hot X-ray emitting intracluster gas ($\sim 10\%$).

Massive galaxy clusters display a whole range of gravitational lensing phenomena, with hosts of objects in the background observable universe acting as sources. Strong lensing by the overall lens potential of the cluster forms multiple images of galaxies (and quasars) primarily behind the central region, some of them in the form of giant arcs (Hennawi et al. 2008). Galaxies in the background of the outer parts of the cluster are weakly lensed by its gravitational field, leading to weak distortions of their appearance as described in Section 6.2. Galaxies in the background of cluster-member galaxies may be strongly lensed by them. Supernovae occurring in multiply imaged background galaxies may be observed repeatedly with large time delays in the individual images (Kelly et al. 2016). Even individual stars in background galaxies may be microlensed by the fine-structure caustic network near the cluster caustic, as shown by Kelly et al. (2018).

As seen from the included example in Figure 6.1, lensing galaxy clusters are spectacular targets for imaging. Abell 370 is one of the clusters studied within the deep-imaging Frontier

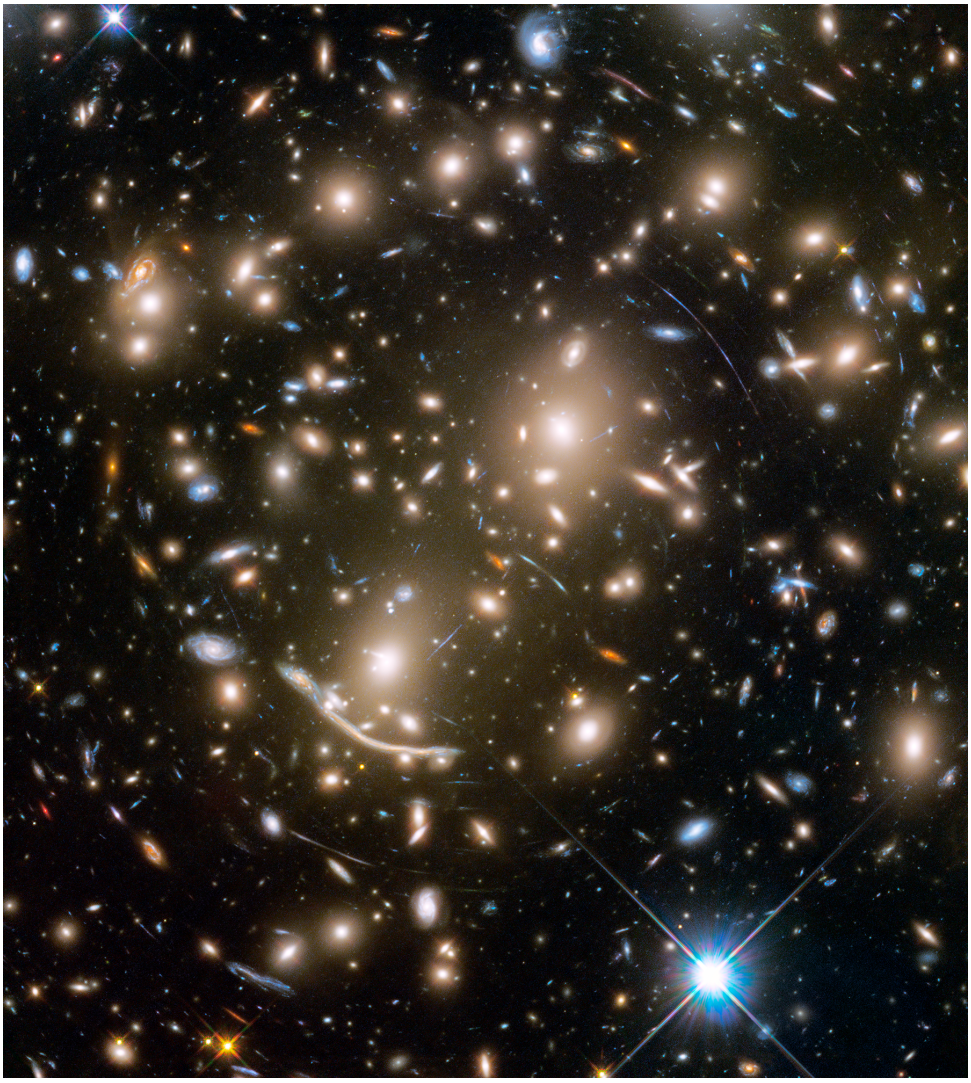

**Figure 6.1:** Galaxy cluster Abell 370 imaged by the Hubble Space Telescope. The thin arcs are images of lensed background galaxies. Image credit: NASA, ESA/Hubble, HST Frontier Fields

Fields survey (Lotz et al. 2017). The image shows the central region of the cluster with numerous cluster-member galaxies (primarily the pale yellow ellipticals), many background galaxies (some at very high redshifts), and some foreground galaxies as well (Lagattuta et al. 2019). The thin arcs with primarily tangential (concentric) orientation scattered throughout the field are strongly lensed background galaxies. The most prominent thicker arc to the lower left of the center can be seen to be formed by multiple images of a background spiral galaxy. A similar background spiral galaxy can be seen to the upper left of the center, in this case strongly lensed by the foreground cluster-member galaxy. For observing background galaxies the cluster

acts as a powerful gravitational telescope, magnifying their angular size so that details of their structure can be studied, and amplifying their flux so that even extremely faint high-redshift galaxies can be detected.

## 6.2 Weak Lensing and Cluster Mass Reconstruction

While the distribution of strongly lensed systems helps to constrain and trace out the distribution of matter in the inner part of the lensing galaxy cluster, weak lensing is crucial for mapping the distribution in the larger outer parts of the cluster.

Weak lensing is based on two assumptions: negligible variation of the lens convergence, shear, and phase on the scale of background galaxy images, and a weak lensing effect of the foreground gravitational field represented by low values of the convergence and shear, $\kappa, \gamma \ll 1$. The first assumption implies that the lens equation is locally well approximated by its linearized version given by Equation (2.14). The geometry of images can be determined from Equation (2.15) using the inverted Jacobian matrix from Equation (2.16) evaluated at the source-center image position $\boldsymbol{\theta}_c$.

Figure 6.2 illustrates the geometry of an image of a circular source formed by the linearized lens equation with convergence $\kappa = 0.1$, shear $\gamma = 0.2$, and phase $\varphi = 120°$. The unit-radius circle in the source plane (left plot) appears in the lens plane (right plot) as an ellipse with semi-major axis $1/|1-\kappa-\gamma|$, semi-minor axis $1/|1-\kappa+\gamma|$, and major axis oriented in the direction of the phase. For $\kappa > 1$ the relative sizes of the semi-axes flip and the major axis is oriented perpendicularly to the phase. Note that the image is deformed and may even be mirrored, but not rotated. For example, the point marked in the figure lying on the source in the direction of the phase appears on the image along the same direction.

With the assumption of low convergence and shear the semi-minor to semi-major axis ratio of the image can be approximated to first order in $\kappa$ and $\gamma$ by $|1-\kappa-\gamma|/|1-\kappa+\gamma| \approx 1-2\,\gamma$. This simple expression shows that the measured axis ratio of the image can yield the local shear value. Although real lensed galaxies cannot be treated as circular sources, a statistical analysis of the axis ratios and orientations of many lensed galaxies in the background of a particular region of the cluster averages out their intrinsic shapes and orientations and yields the shear

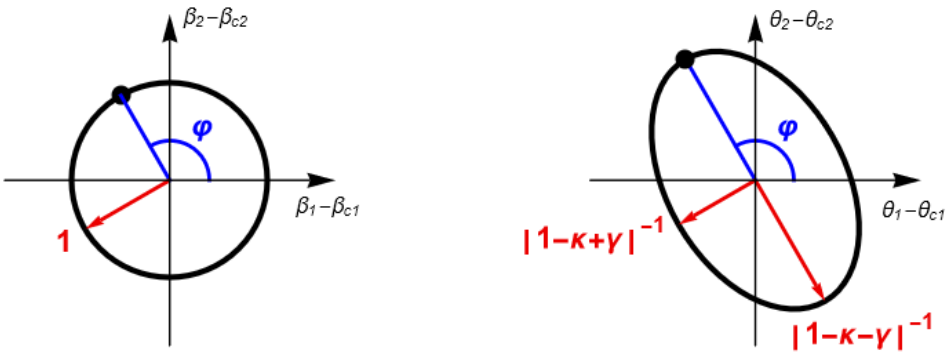


**Figure 6.2:** Imaging by the linearized lens equation. A unit-radius circular source (left panel) appears as an elliptical image (right panel) with the sizes and orientations of its semi-axes marked in the figure. Illustrated for convergence $\kappa = 0.1$, shear $\gamma = 0.2$, and phase $\varphi = 120°$.

and phase of the foreground gravitational field. For a sufficiently high number of background galaxies, lens-plane maps of $\gamma \cos 2\varphi$ and $\gamma \sin 2\varphi$ can be constructed. Fourier transformation of Equation (2.11) and Equation (2.9) shows that the Fourier images of these maps can be used to compute the Fourier image of $\kappa$. Transformation back to real space yields the convergence $\kappa(\boldsymbol{\theta})$, which provides a map of the surface density of the lensing galaxy cluster.

This bird's-eye-view description indicates the basic principle of the method for mapping the mass distribution of the cluster from image shapes of background galaxies, originally developed by Kaiser & Squires (1993). While several clusters had been analyzed earlier using other techniques, most subsequent weak-lensing cluster mass reconstructions have been based on variants of the Kaiser–Squires algorithm. Examples of clusters with mass distributions mapped by weak lensing include Abell 2218 (Squires et al. 1996) or Abell 2163 (Squires et al. 1997). A weak-lensing analysis of 50 galaxy clusters by Okabe et al. (2013) showed that the average cluster density distribution closely followed the Navarro–Frenk–White profile (Navarro et al. 1997), as predicted by cosmological structure-formation simulations of a cold dark matter universe.

Arguably the most famous result was obtained by Clowe et al. (2004), who mapped the cluster 1E 0657-558 (the Bullet Cluster) consisting of two subclusters separated after a head-on collision. The results showed that the total matter distribution (dominated by dark matter) peaked at positions offset from the peaks of the baryonic matter distribution (dominated by X-ray emitting intracluster gas). The dark matter peaks coincided with the concentrations of

galaxies of the subclusters, while their intracluster gas distributions lagged behind, slowed down by their super-sonic collision indicated by an observed shock front. In addition to demonstrating the different distribution of dark and baryonic matter, the analysis illustrated the collision-less nature of dark matter. Using numerical simulations of the colliding subclusters, Randall et al. (2008) derived an upper limit on the self-interaction cross section of dark matter particles. The properties of the Bullet Cluster are hard to explain by alternative theories assuming only baryonic matter with an altered description of gravitation.

While the early cluster mass reconstructions were based purely on weak lensing, more state-of-the-art approaches combine the weak-lensing data with analyses of strong lensing. While the former provide information on the large-scale distribution, particularly in the outer regions of the cluster, the latter provide better constraints for the mass distribution in the central region. Cluster mass distribution maps based on the combined analysis are available for a number of clusters, including the Bullet Cluster (Bradač et al. 2006) or Abell 370 (Strait et al. 2018). One of the goals of such reconstructions is to improve the spatial resolution of the maps, in order to study the finer structure and populations of substructures in the matter distribution.

For weak lensing this requires a larger number of detected background galaxies to improve the statistical analysis. In the inner regions of the cluster this requires a careful analysis to detect signatures of "galaxy-galaxy" strong-lensing systems. A detailed analysis of 11 galaxy clusters by Meneghetti et al. (2020) revealed a surprisingly high number of such systems, indicating a lensing efficiency of the corresponding substructures much higher than expected from clusters formed in cold dark matter simulations. Further research will show whether this very recent result just reflects some overlooked issue in the analysis or it stands up to scrutiny and poses a challenge to current structure-formation simulations.

## 6.3 Included Papers on Cluster Lensing

In the fifth included paper (Karamazov et al. 2021, Appendix E) we explore gravitational lensing by a single point mass embedded in a spherically symmetric Navarro–Frenk–White dark-matter halo. This extremely simple model can serve as a starting point for studying the influence of compact substructures on the lensing by the large-scale distribution of matter in a galaxy-

cluster halo. Lensing by the model can be studied analytically and the low number of parameters permits a systematic exploration of its parameter space. In this paper we concentrate on the structure of the critical curves and caustics of the model as a function of mass and radial position of the point mass within the halo. Initial tests revealed an unexpected richness of critical-curve topologies and caustic structures, as illustrated by the galleries in Figures 5.A and 5.B. We found that point masses heavier than a critical mass (about $4 \cdot 10^{-4}$ of the halo mass) are strong enough to suppress the radial critical curve and caustic of the halo when positioned at its center. We mapped the boundaries between different critical curve topologies in the point-mass parameter space, with Figure 6 showing their overall complex structure. The corresponding caustics undergo many different metamorphoses, including lips and elliptic, hyperbolic and parabolic umbilics, with several examples demonstrated in detail. Overall, although lower masses affect smaller areas of the lens plane, the corresponding changes of the critical curve and caustic with position are more complex than for higher masses. In Appendix B we illustrate the peculiar properties of the radial critical curve and caustic (linear but not a fold) in the case of the critical mass.

In the sixth included paper (Karamazov & Heyrovský 2021, Appendix F) we study the same model, this time exploring its shear, phase, and image geometry. We derive formulae for the combined shear and phase and illustrate the involved geometry. We describe the occurrence of zero-shear points and identify the conditions when they form umbilic points. We present grids of image-plane maps of the shear, phase, and their weak-lensing approximation for the same combinations of point-mass parameters as in Appendix E. We include also grids of plots of relative deviations of the different quantities to illustrate the perturbing effect of the point mass, or the relative error introduced by the weak-lensing approximation. We introduce in Figure 14 the convergence–shear diagram as a new tool for visualizing the geometries of small-source images formed by a gravitational lens anywhere in the image plane. We demonstrate its usage on an unperturbed NFW halo in Figure 3, and utilize them to illustrate the properties of images formed by our model in Figures 8.A and 8.B. We discuss the implications and relevance of our results for more realistic lens models.

# Chapter 7

## Conclusions

The papers included in this collection present a sample of the outcome of our ongoing study of gravitational lensing. In each of them we achieved new results and provided answers to some of the initially formulated questions. At the same time, each of them opened up new questions and new problems to be explored. We conclude here by mentioning at least some open questions and directions of further research for the three presented topics.

One of the main questions left unanswered by our triple-lens research is how many lensing regimes does the triple lens have? If we define the regimes by their critical-curve topology, we found a total of eleven in comparison with the three regimes of the two-point-mass lens. Interestingly, the number of regimes depends on the combination of masses. Of the three combinations studied in detail in Appendix C, the equal-mass triple has nine regimes while the planet-in-binary and the star-planet-moon triples have eleven. While the demonstrated parameter-space mapping reveals all regimes for a given combination of masses, the sample results cannot guarantee that no other regime would appear for a different combination.

In principle, one could employ a similar method using different three parameters of the lens, such as keeping the shape of the configuration fixed while varying the relative masses and the perimeter of the configuration. However, this would add just different three-dimensional cuts through the five-dimensional parameter space. In other words, even a combination with this approach would not provide a full mapping of the parameter space of the lens. Nevertheless, there may be other methods to identify the range of possible critical-curve topologies, for example by studying the sequences of transitions occurring from the close to the wide limit,

guided by the structure of the Jacobian as a surface over the lens plane. The answer seems elusive, but it may well be within reach.

In our quasar microlensing research on the changing X-ray line-profile features in the course of a caustic crossing event, we demonstrated the effects occurring for an accretion disk surrounding a maximally rotating Kerr black hole. A study of the effects for a central black hole with a different spin parameter (including a Schwarzschild black hole) is currently underway. In such a case the innermost stable circular orbit (ISCO) defining the inner edge of the disk lies outside the horizon instead of coinciding with it. The caustic position with respect to the ISCO then plays an additional role, generating distinct line-profile features. The overall variability of the line profile can be expected to be even higher, possibly yielding a sequence of microlensed profiles during a caustic crossing similar to those detected by Chartas et al. (2012). This can then be shown by exploring the sequences of line-profile changes within the studied model.

Our exploration of the lensing impact of massive objects in a dark matter halo offers many possible enhancements of the studied elementary model of a point-mass lens in a spherical NFW halo. For example, replacing the point mass with a dark matter subhalo (spherical or elliptical), or exploring the combined influence of two objects to identify the conditions under which they generate independent critical-curve and caustic features or more complex combined features. At present we are carrying out simulations of lensing by a NFW cluster halo with a population of ellipsoidal subhalos (better galaxy model than a point mass), generating plots of the critical curves, caustics, maps of the shear, phase, and the other quantities studied in Appendix F. By comparing the results with those of the systematically explored simple model presented here we hope to achieve better understanding of the specific lensing impact of different substructures.

# References


Abe, F., Allen, W., Banks, T., et al. 1997, in IAP Astrophysics Colloquium 12, Variable Stars and the Astrophysical Returns of Microlensing Surveys, ed. R. Ferlet, J. P. Maillard, & B. Raban (Gif-sur-Yvette: Editions Frontières), 75

Alard, C. & Guibert, J. 1997, Astronomy & Astrophysics, 326, 1

Albrow, M., Beaulieu, J.-P., Birch, P., et al. 1998, The Astrophysical Journal, 509, 687

Alcock, C., Allsman, R. A., Alves, D., et al. 1997, The Astrophysical Journal, 479, 119

Alcock, C., Allsman, R. A., Alves, D., et al. 2000, The Astrophysical Journal, 541, 270

Alloin, D., Johnson, R., & Lira, P. 2006, Physics of Active Galactic Nuclei at all Scales, Lecture Notes in Physics 693, ed. D. Alloin, R. Johnson, & P. Lira (Berlin and Heidelberg: Springer)

Beaulieu, J.-P., Bennett, D. P., Batista, V., et al. 2016, The Astrophysical Journal, 824, 83

Beaulieu, J.-P., Bennett, D. P., Fouqué, P., et al. 2006, Nature, 439, 437

Bennett, D. P., Anderson, J., Bond, I. A., et al. 2006, The Astrophysical Journal Letters, 647, L171

Bennett, D. P., & Rhie, S. H. 1996, The Astrophysical Journal, 472, 660

Bennett, D. P., Rhie, S. H., Nikolaev, S., et al. 2010, The Astrophysical Journal, 713, 837

Bennett, D. P., Rhie, S. H., Udalski, A., et al. 2016, The Astronomical Journal, 152, 125

Bennett, D. P., Udalski, A., Bond, I. A., et al. 2020, The Astronomical Journal, 160, 72

Bond, I. A., Udalski, A., Jaroszyński, M., et al. 2004, The Astrophysical Journal Letters, 606, L155

Bradač, M., Clowe, D., Gonzalez, A. H., et al. 2006, The Astrophysical Journal, 652, 937

Cassan, A., Beaulieu, J.-P., Fouqué, P., et al. 2006, Astronomy & Astrophysics, 460, 277

Cassan, A., Kubas, D., Beaulieu, J.-P., et al. 2012, Nature, 481, 167

Chartas, G., Kochanek, C. S., Dai, X., et al. 2012, The Astrophysical Journal, 757, 137

Chen, B., Dai, X., Kochanek, C. S., et al. 2012, The Astrophysical Journal, 755, 24

Choi, J.-Y., Shin, I.-G., Park, S.-Y., et al. 2012, The Astrophysical Journal, 751, 41

Clowe, D., Gonzalez, A., & Markevitch, M. 2004, The Astrophysical Journal, 604, 596

Congdon, A. B. & Keeton, C. 2018, Principles of Gravitational Lensing (Cham: Springer)

Daněk, K. & Heyrovský, D. 2015a, The Astrophysical Journal, 806, 63 (App. A)

Daněk, K. & Heyrovský, D. 2015b, The Astrophysical Journal, 806, 99 (App. B)

Daněk, K. & Heyrovský, D. 2019, The Astrophysical Journal, 880, 72 (App. C)

Deguchi, S. & Watson, W. D. 1986, Physical Review D, 34, 1708

Dodelson, S. 2017, Gravitational Lensing (Cambridge: Cambridge University Press)

Dominik, M., Jørgensen, U. G., Rattenbury, N. J., et al. 2010, Astronomische Nachrichten, 331, 671

Duchêne, G. & Kraus, A. 2013, Annual Review of Astronomy and Astrophysics, 51, 269

Eigenbrod, A., Courbin, F., Meylan, G., et al. 2008, Astronomy & Astrophysics, 490, 933

Einstein, A. 1936, Science, 84, 506

Erdl, H. & Schneider, P. 1993, Astronomy & Astrophysics, 268, 453

Fouqué, P., Heyrovský, D., Dong, S., et al. 2010, Astronomy & Astrophysics, 518, A51

Gaudi, B. S. 2021, arXiv:2102.01715

Gaudi, B. S., Bennett, D. P., Udalski, A., et al. 2008, Science, 319, 927

Gould, A., Dong, S., Gaudi, B. S., et al. 2010, The Astrophysical Journal, 720, 1073

Gould, A., Udalski, A., Shin, I.-G., et al. 2014, Science, 345, 46

Han, C. 2008, The Astrophysical Journal, 684, 684

Han, C., Bennett, D. P., Udalski, A., et al. 2019, The Astronomical Journal, 158, 114

Han, C. & Han, W. 2002, The Astrophysical Journal, 580, 490

Han, C., Lee, C.-U., Udalski, A., et al. 2020, The Astronomical Journal, 159, 48

Han, C., Udalski, A., Choi, J.-Y., et al. 2013, The Astrophysical Journal Letters, 762, L28

Han, C., Udalski, A., Gould, A., et al. 2017, The Astronomical Journal, 154, 223

Han, C., Udalski, A., Kim, D., et al. 2021, The Astronomical Journal, 161, 270

Hennawi, J. F., Gladders, M. D., Oguri, M., et al. 2008, The Astronomical Journal, 135, 664

Herlt, E. & Stephani, H. 1976, International Journal of Theoretical Physics, 15, 45

Heyrovský, D. 2003, The Astrophysical Journal, 594, 464

Heyrovský, D. 2005, The Astrophysical Journal, 624, 28

Heyrovský, D. 2008, in Proceedings of the Manchester Microlensing Conference, ed. E. Kerins, S. Mao, N. Rattenbury, & Ł. Wyrzykowski (Manchester: University of Manchester), PoS(GMC8)028

Heyrovský, D. & Sasselov, D. 2000, The Astrophysical Journal, 529, 69

Heyrovský, D., Sasselov, D., & Loeb, A. 2000, The Astrophysical Journal, 543, 406

Jaroszyński, M. 2002, Acta Astronomica, 52, 39

Jaroszyński, M., Skowron, J., Udalski, A., et al. 2006, Acta Astronomica, 56, 307

Jaroszyński, M., Skowron, J., Udalski, A., et al. 2010, Acta Astronomica, 60, 197

Jaroszyński, M., Udalski, A., Kubiak, M., et al. 2004, Acta Astronomica, 54, 103

Johnson, S. A., Penny, M., Gaudi, B. S., et al. 2020, The Astronomical Journal, 160, 123

Kaiser, N. & Squires, G. 1993, The Astrophysical Journal, 404, 441

Karamazov, M., & Heyrovský, D. 2021, The Astrophysical Journal, submitted, arXiv:2109.02495 (App. F)

Karamazov, M., Timko, L., & Heyrovský, D. 2021, The Astrophysical Journal, accepted, arXiv:2103.16965 (App. E)

Kassiola, A. & Kovner, I. 1993, The Astrophysical Journal, 417, 450

Kayser, R., Refsdal, S., & Stabell, R. 1986, Astronomy & Astrophysics, 166, 36

Keeton, C. R. & Kochanek, C. S. 1998, The Astrophysical Journal, 495, 157

Kelly, P. L., Diego, J. M., Rodney, S., et al. 2018, Nature Astronomy, 2, 334

Kelly, P. L., Rodney, S. A., Treu, T., et al. 2016, The Astrophysical Journal Letters, 819, L8

Khavinson, D., & Neumann, G. 2006, Proceedings of the American Mathematical Society, 134, 1077

Kim, S.-L., Lee, C.-U., Park, B.-G., et al. 2016, Journal of the Korean Astronomical Society, 49, 37

Lagattuta, D. J., Richard, J., Bauer, F. E., et al. 2019, Monthly Notices of the Royal Astronomical Society, 485, 3738

Ledvina, L., Heyrovský, D., & Dovčiak, M. 2018, The Astrophysical Journal, 863, 66 (App. D)

Liebes, S. 1964, Physical Review, 133, 835

Liebig, C. & Wambsganss, J. 2010, Astronomy & Astrophysics, 520, A68

Lotz, J. M., Koekemoer, A., Coe, D., et al. 2017, The Astrophysical Journal, 837, 97

Mao, S. & Paczyński, B. 1991, The Astrophysical Journal Letters, 374, L37

Massey, R., Rhodes, J., Ellis, R., et al. 2007, Nature, 445, 286

Meneghetti, M., Davoli, G., Bergamini, P., et al. 2020, Science, 369, 1347

Metcalf, R. B., Meneghetti, M., Avestruz, C., et al. 2019, Astronomy & Astrophysics, 625, A119

Navarro, J. F., Frenk, C. S., & White, S. D. M. 1997, The Astrophysical Journal, 490, 493

Nye, J. F. 1999, Natural Focusing and Fine Structure of Light: Caustics and Wave Dislocations (Bristol, Philadelphia: Institute of Physics Publishing)

Okabe, N., Smith, G. P., Umetsu, K., et al. 2013, The Astrophysical Journal Letters, 769, L35

Paczyński, B. 1986, The Astrophysical Journal, 304, 1

Paczyński, B. 1991, The Astrophysical Journal Letters, 371, L63

Pejcha, O. & Heyrovský, D. 2009, The Astrophysical Journal, 690, 1772

Penny, M. T., Gaudi, B. S., Kerins, E., et al. 2019, The Astrophysical Journals, 241, 3

Petters, A. O., Levine, H., & Wambsganss, J. 2001, Singularity Theory and Gravitational Lensing (Boston: Birkhäuser)

Planck Collaboration, Ade, P. A. R., Aghanim, N., et al. 2014, Astronomy & Astrophysics, 571, A17

Planck Collaboration, Aghanim, N., Akrami, Y., et al. 2020, Astronomy & Astrophysics, 641, A8

Poleski, R., Skowron, J., Udalski, A., et al. 2014, The Astrophysical Journal, 795, 42

Popowski, P., Griest, K., Thomas, C. L., et al. 2005, The Astrophysical Journal, 631, 879

Randall, S. W., Markevitch, M., Clowe, D., et al. 2008, The Astrophysical Journal, 679, 1173

Refsdal, S. 1964, Monthly Notices of the Royal Astronomical Society, 128, 295

Renault, C., Afonso, C., Aubourg, E., et al. 1997, Astronomy & Astrophysics, 324, L69

Rhie, S. H. 2003, arXiv:astro-ph/0305166

Schmidt, R. W. & Wambsganss, J. 2010, General Relativity and Gravitation, 42, 2127

Schneider, P., Ehlers, J., & Falco, E. E. 1992, Gravitational Lenses (Berlin: Springer-Verlag)

Schneider, P., Kochanek, C., & Wambsganss, J. 2006, Gravitational Lensing: Strong, Weak and Micro (Berlin: Springer)

Schneider, P. & Weiss, A. 1986, Astronomy & Astrophysics, 164, 237

Skowron, J., Jaroszyński, M., Udalski, A., et al. 2007, Acta Astronomica, 57, 281

Sluse, D., Schmidt, R., Courbin, F., et al. 2011, Astronomy & Astrophysics, 528, A100

Spergel, D., Gehrels, N., Baltay, C., et al. 2015, arXiv:1503.03757

Squires, G., Kaiser, N., Babul, A., et al. 1996, The Astrophysical Journal, 461, 572

Squires, G., Neumann, D. M., Kaiser, N., et al. 1997, The Astrophysical Journal, 482, 648

Stockton, A. 1980, The Astrophysical Journal Letters, 242, L141

Strait, V., Bradač, M., Hoag, A., et al. 2018, The Astrophysical Journal, 868, 129

Sumi, T., Woźniak, P. R., Udalski, A., et al. 2006, The Astrophysical Journal, 636, 240

Suzuki, D., Bennett, D. P., Udalski, A., et al. 2018, The Astronomical Journal, 155, 263

Tisserand, P., Le Guillou, L., Afonso, C., et al. 2007, Astronomy & Astrophysics, 469, 387

Tsapras, Y., Street, R., Horne, K., et al. 2009, Astronomische Nachrichten, 330, 4

Tsapras, Y., Street, R. A., Hundertmark, M., et al. 2019, Publications of the Astronomical Society of the Pacific, 131, 124401

Udalski, A., Szymański, M., Kałużny, J., et al. 1997, Acta Astronomica, 47, 169

Vermaak, P. 2000, Monthly Notices of the Royal Astronomical Society, 319, 1011

Virbhadra, K. S. & Ellis, G. F. R. 2000, Physical Review D, 62, 084003

Walsh, D., Carswell, R. F., & Weymann, R. J. 1979, Nature, 279, 381

Wambsganss, J. 1999, Journal of Computational and Applied Mathematics, 109, 353

Wambsganss, J., Witt, H. J., & Schneider, P. 1992, Astronomy & Astrophysics, 258, 591

Witt, H. J. 1990, Astronomy & Astrophysics, 236, 311

Witt, H. J., & Mao, S. 1994, The Astrophysical Journal, 430, 505

Young, P., Gunn, J. E., Kristian, J., et al. 1980, The Astrophysical Journal, 241, 507

Zwicky, F. 1937, Physical Review, 51, 290

# Appendix A

## Image-plane Analysis of $n$-Point-mass Lens Critical Curves and Caustics

Daněk, K., & Heyrovský, D. 2015a. The Astrophysical Journal, Vol. 806, Art. 63.
DOI:10.1088/0004-637X/806/1/63
https://ui.adsabs.harvard.edu/abs/2015ApJ...806...63D

# Appendix B

## Critical Curves and Caustics of Triple-lens Models

Daněk, K., & Heyrovský, D. 2015b. The Astrophysical Journal, Vol. 806, Art. 99.

DOI:10.1088/0004-637X/806/1/99

https://ui.adsabs.harvard.edu/abs/2015ApJ...806...99D

# Appendix C

## Triple-lens Gravitational Microlensing:

## Critical Curves for Arbitrary Spatial Configuration

Daněk, K., & Heyrovský, D. 2019. The Astrophysical Journal, Vol. 880, Art. 72.

DOI:10.3847/1538-4357/ab2982

https://ui.adsabs.harvard.edu/abs/2019ApJ...880...72D

# Appendix D

## X-Ray Line Profile Variations during Quasar Microlensing

Ledvina, L., Heyrovský, D., & Dovčiak, M. 2018. The Astrophysical Journal, Vol. 863, Art. 66
DOI:10.3847/1538-4357/aad0f3
https://ui.adsabs.harvard.edu/abs/2018ApJ...863...66L

# Appendix E

## Gravitational Lensing By a Massive Object in a Dark Matter Halo. I. Critical Curves and Caustics

Karamazov, M., Timko, L., & Heyrovský, D., 2021. The Astrophysical Journal, accepted

Preprint arXiv:2103.16965

https://ui.adsabs.harvard.edu/abs/2021arXiv210316965K

# Appendix F

## Gravitational Lensing By a Massive Object in a Dark Matter Halo. II. Shear, Phase, and Image Geometry

Karamazov, M., & Heyrovský, D., 2021. The Astrophysical Journal, submitted

Preprint arXiv:2109.02495

https://ui.adsabs.harvard.edu/abs/2021arXiv210902495K